

Quasi Fe MIL-53 nanozyme inducing ferroptosis and immunogenic cell death for cancer immunotherapy

Received: 6 March 2024

Accepted: 26 February 2025

Published online: 07 March 2025



Zihui Yan¹, Yang Bai¹✉, Songtao Zhang², Lingyi Kong³, Yu Wang³, Huilin Sun¹, Yi Li¹, Lin Qiu¹, Ruijie Zhang¹, Pengju Jiang¹, Donghui Zhao¹, Zhongyan Chen⁴, Yafei Li^{1,3}✉, Huan Pang²✉ & Jianhao Wang^{1,5}✉

Nanozymes offer diverse therapeutic potentials for cancer treatment which is dependent on the development of nanomaterials. Quasi-metal-organic framework is a class of metal-organic framework-derived nanomaterials with a transition state from metal-organic frameworks towards metal oxide featuring porous structure and high activity. Herein an iron-based quasi-metal-organic framework nanozyme Q-MIL-53(Fe) is reported via a controlled deligandation strategy, exhibiting enhanced peroxidase-/catalase-mimic activity and glutathione depletion capacity, whose underlying mechanisms are studied via density functional theory calculations. Q-MIL-53(Fe) demonstrates biocompatibility and superior antitumor efficacy compared to pristine MIL-53(Fe). It can activate antitumor immune response by inducing ferroptosis and immunogenic cell death, promoting dendritic cell maturation and T lymphocytes infiltration. Furthermore, a combination of Q-MIL-53(Fe) and programmed cell death protein 1 antibody amplifies cancer immunotherapy. This study validates the antitumor activity of quasi-metal-organic frameworks and its immunotherapy induction potential. It would broaden the application of quasi-metal-organic frameworks and open avenues for developing antitumor nanozymes.

Cancer remains a prominent factor in causing fatalities of death universally in spite of great progress in treatment over recent decades^{1,2}. Conventional cancer therapies such as chemotherapy, radiotherapy and surgery are often limited by severe side effects and the development of drug resistance in tumors^{3,4}. There is an urgent need to develop more effective and safer therapeutic strategies for cancer⁵. Ferroptosis has attracted tremendous attention in cancer therapy as an emerging regulated cell death combined with iron-mediated lipid peroxidation^{6,7}. In the process of ferroptosis, the downregulation of

glutathione (GSH) leads to glutathione peroxidase 4 (GPX4) deactivation and imbalance in cellular antioxidant capacity, causing lipid peroxides (LPO) dysfunction with excessive reactive oxygen species (ROS)^{8,9}. The unique characteristics evade resistance to apoptosis/necroptosis and induce ferroptosis. More importantly, during the process of ferroptosis, there is typically the release of damage-associated molecular patterns (DAMPs), which possess the capacity to induce immunogenic cell death (ICD). It plays a vital role in triggering immune responses against tumor growth^{10,11}. These signals contribute

¹School of Pharmacy, Changzhou University, Changzhou 213164, P. R. China. ²School of Chemistry and Chemical Engineering, Yangzhou University, Yangzhou 225002, P. R. China. ³Jiangsu Collaborative Innovation Centre of Biomedical Functional Materials, School of Chemistry and Materials Science, Nanjing Normal University, Nanjing 210023, P. R. China. ⁴College of Chemistry and Materials Engineering, Wenzhou University, Wenzhou 325035, P. R. China. ⁵School of Medical and Health Engineering, Changzhou University, Changzhou 213164, P. R. China. ✉e-mail: baiy@cczu.edu.cn; liyafei@njnu.edu.cn; huanpangchem@hotmail.com; minuswan@cczu.edu.cn

to improving tumor immunogenicity on dendritic cells (DCs), resulting in the activation of tumor-specific T lymphocytes and the initiation of antitumor immune responses¹². Therefore, ferroptosis and ICD are believed as promising strategies to enhance the therapeutic effect by evoking a specific antitumor immunity¹³.

Nanozymes are nanomaterials with intrinsic enzyme-like activities that catalyze biochemical reactions under physiological conditions^{14,15}. Nanozymes possess advantages over natural enzymes including high stability and low cost. More importantly, the composition, structure, and morphology of nanozymes could be designed to exhibit multiple redox reactive enzyme-like activities, including peroxidase (POD), catalase (CAT), superoxide dismutase (SOD), oxidase (OXD), etc. Thus, the regulation of ROS levels endows nanozymes potent for multimodal antitumor therapeutics¹⁶.

Since Fe₃O₄ nanoparticles (NPs) were reported to have intrinsic horseradish peroxidase (HRP)-like biocatalytic activity, they have been universally utilized as nanozymes for tumor treatment¹⁷. The mechanism of Fe₃O₄ as nanozyme in tumor inhibition can be understood mainly as a Fenton reaction, which catalyzes excessive H₂O₂ in the tumor microenvironment (TME) via Fe³⁺/Fe²⁺ ions to generate excessive toxic ·OH or other radicals. Tremendous interests have been attracted to the morphological, structural, or compositional designing of iron based nanozyme for approaching more efficient tumor inhibition.

As one of the most popular classes of nanomaterials designed for nanozymes, metal-organic frameworks (MOF), also known as coordination polymers (CP), offer multitudinous platforms for the design of metal-based nanozymes^{18,19}. MOF assembles metal ions/nodes and organic ligands into coordination networks^{20,21}. The abundant enzyme-mimicking catalytic sites together with tunable pore structure make MOF an ideal candidate as an antitumor nanozyme. However, pristine MOF suffers from low stability in the physiological environment, sufficient activity, or finite enzyme-like varieties, which hinders its direct use. Further functionalizations such as structure exploration²², composition^{23–25} and derivation^{26,27} have been proven to be efficient strategies. MOF has acted as sacrificing templates to be etched or pyrolyzed for the fabrication of diverse derivatives such as metal oxides and highly porous carbon-based material doping with heteroatoms, metal or metal oxides, depending on the derivation conditions²⁸. The MOF-derived nanomaterials benefit from the inherited morphologies, porosity, large surface areas, and tunable structures, which are all contributing to the catalytic performance elevation. The enhanced stability against acidic aqueous conditions and biothiols enables them usable in the physiological environments especially TME. Liu et al. developed a controllable fabrication of iron-based single-atom nanozymes (SAzymes) FeN₅ via a melamine-mediated pyrolysis activation with ZIF-8, a Zn based MOF, as template. The optimized five-coordinated Fe-N coordination structure endowed FeN₅ SAzyme 3.45 × 10⁵-fold POD-like activity enhancement compared to Fe₃O₄ nanozyme as well as reinforced antitumor effect in vitro and in vivo²⁹.

Quite different from other derivatives of MOF, quasi-MOF contains a partially broken connection between the metal nodes and organic ligands^{30,31}. Quasi-MOF is fabricated via controlled deligandation of MOF precursor to establish accessible M-O sites without interrupting the porous structure³². The partial removal of the organic ligands exposes mass active interfaces and offers accessibility for interactions with substrate³³. Xu et al. proposed at 2018 for the first time the formation of quasi-MOF through controlled deligandation via thermal transformation of the metal/MOF composites. The quasi-MOF was proved to be the transition-state nanostructure between MOF and metal oxide. The porous structure and strengthened metal nanoparticle/MOF interactions resulted in significantly enhanced catalytic activity in the low-temperature oxidation of carbon monoxide (CO)³⁰. Chen et al. developed Zn-based quasi-MOF nanospheres via solvent-assisted ligand exchange which was characterized as hierarchical

structure with efficient exposure of Zn nodes and dynamic structure evolution of active sites. When utilized as sulfur electrocatalyst in lithium-sulfur batteries, it provided sufficient active sites to improve sulfur confinement and LiPs interaction³⁴. The extensive application of quasi-MOF in heterogeneous catalysis and energy storage inspired us to explore their therapeutic efficiency in tumor treatment which has been barely reported by now. The fabrication of antitumor quasi-MOF nanozymes not only requests the elaborate control of the deligandation condition, but also need to meet the requirement of biosafety, enzymatic activity and appropriate size.

Herein we report an iron-based quasi MOF nanozyme Q-MIL-53(Fe) through a controlled deligandation process, which involves thermal treatment of MIL-53(Fe) at specific temperatures. The partial deligandation aimed to introduce more accessible Fe-O sites within the MOF structure, which was characterized via X-ray absorption spectroscopy (XAS), X-ray photoelectron spectroscopy (XPS), etc. The Q-MIL-53(Fe) exhibited enhanced POD-/CAT-mimic and GSH depletion compared to the pristine MOF and completely derived Fe₃O₄-doping porous carbon materials. The underlying catalysing mechanisms were illustrated via density functional theory (DFT) calculations. Q-MIL-53(Fe) exhibited biocompatibility and demonstrated superior antitumor efficacy compared to pristine MIL-53(Fe) in vitro and in vivo. Further study revealed that Q-MIL-53(Fe) could induce LPO accumulation and ferroptosis via ROS generation, GSH consumption and mitochondrial dysfunction. ICD has also been confirmed via calreticulin (CRT) exposure, high mobility group protein B1 (HMGB1) release, and adenosine triphosphate (ATP) secretion. Moreover, Q-MIL-53(Fe) treatment led to DC mutation and T-cell infiltration, suggesting its potential to trigger tumor immune response. The combination of Q-MIL-53(Fe) with anti-programmed cell death ligand 1 (anti-PD-L1, αPD-L1) exhibited enhanced tumor elimination and metastasis suppression over free antibodies and Q-MIL-53(Fe) therapy alone. This study validated for the first time the capability of antitumor activity, ferroptosis/ICD induction and cancer immunotherapy of iron-based quasi MOF nanozyme. It would provide more application potential of quasi MOF and contribute to the designing and development of antitumor nanozymes.

Results and Discussion

Morphological characterizations

The synthesis of MIL-53(Fe) is illustrated in Fig. 1a. Briefly, MIL-53(Fe) was obtained via a solvothermal method using FeCl₃·6H₂O and terephthalic acid in N, N-dimethylacetamide (DMA). Thermogravimetric analysis (TGA) of the synthesized MIL-53(Fe) revealed two transition points at around 350 and 400 °C, between which the MOF nanostructures started to disintegrate. Thus 350 and 400 °C were referred to as the temperatures for the controlled step-by-step deligandation (Fig. 1b). Calcination temperature of 500 °C was also selected as the sample representing completely derived MOF. Then MIL-53(Fe) was calcinated at 350, 400, and 500 °C, respectively, for 1 h under N₂ atmosphere, which were denoted as Q-MIL-53(Fe), MIL-53(Fe)-400, and MIL-53(Fe)-500 (Supplementary Fig. 1).

The scanning electron microscopy (SEM) images disclosed the fusiform morphology of MIL-53(Fe) with dimensions of 340 nm in length and 90 nm in width, which were suitable for further in vivo applications (Fig. 2a). The nanoparticles obtained via calcination at 350 and 400 °C maintained the size and the fusiform morphology of the pristine MIL-53(Fe) (Fig. 2b and c). As the calcination temperature increased to 500 °C, the sample was narrowed compared to the pristine MOF, as well as a rough surface of the substrate and the surficial emergence of nanoparticles (Fig. 2d). It indicated that the MOF was gradually disrupted. The morphological variations of the MIL-53(Fe), Q-MIL-53(Fe), MIL-53(Fe)-400, and MIL-53(Fe)-500 are further revealed by transmission electron microscopy (TEM) images (Fig. 2e–l). The TEM analysis showed that Q-MIL-53(Fe) inherited the structural

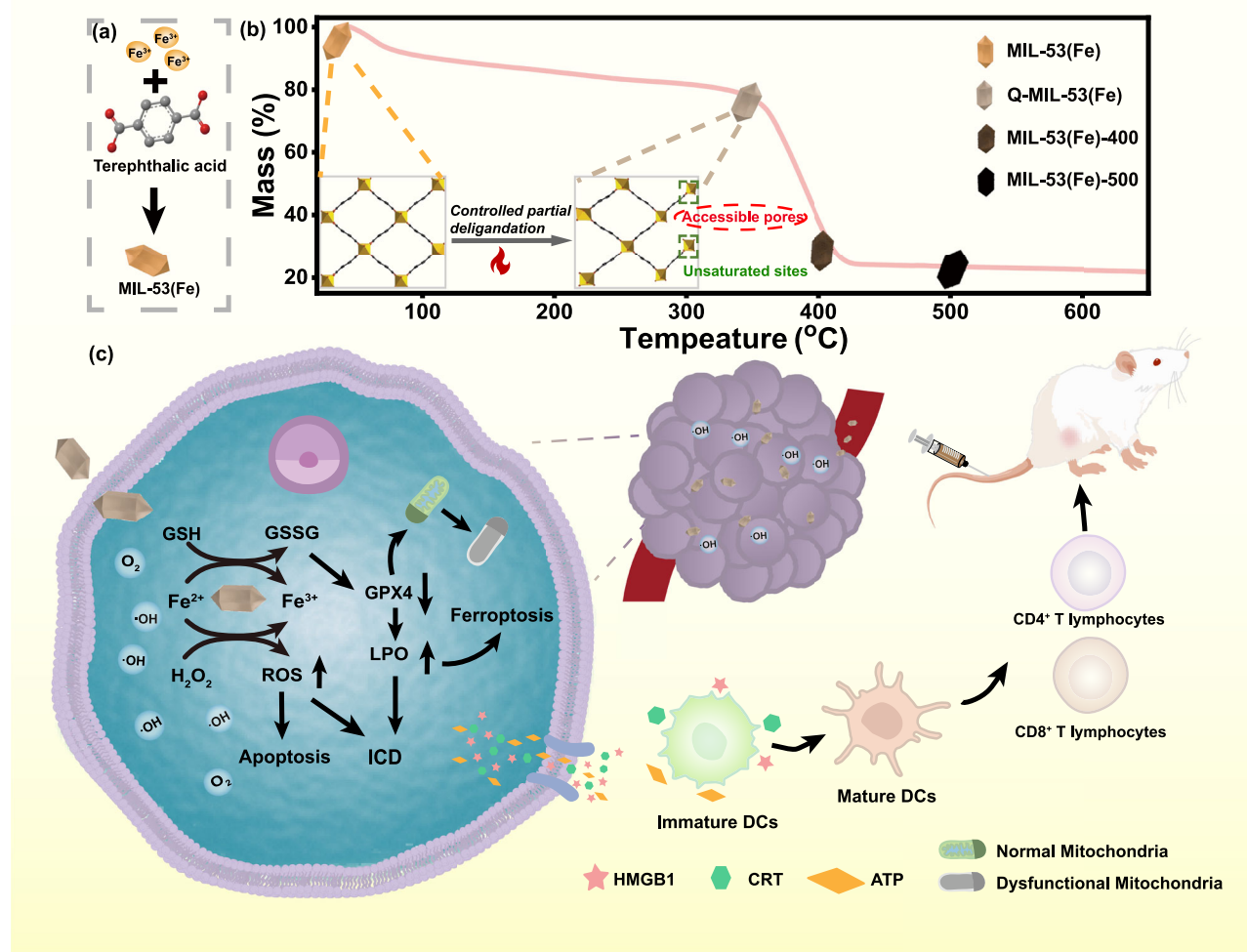


Fig. 1 | Schematic illustrations. Schematic illustrations of (a) the synthesis of MIL-53(Fe), (b) controlled deligandation and step-by-step thermal treatment to obtain the derivatives of MIL-53(Fe) and (c) its intracellular therapeutic mechanisms.

skeleton of MIL-53(Fe) without surficial nanoparticles generation (Fig. 2f and j). While MIL-53(Fe)-400 exhibited rough surface and irregular nanoparticles (Fig. 2g and k). The original fusiform particles could barely be seen in MIL-53(Fe)-500, which exhibited the fusiform agglomerate of rhombic nanoparticles with definite edges instead (Fig. 2h and l). The high-resolution TEM (HRTEM) images of MIL-53(Fe) and Q-MIL-53(Fe) could hardly show any lattice fringe, which suggests that they tended to be unstable under the high-energy electron beam (Fig. 2m and n). The dim holes in the selected area electron diffraction (SAED) images also indicated the poor crystallinity (insets of Fig. 2m and n). The results revealed the controlled deligandation at a relatively low temperature of 350 °C is insufficient for MIL-53(Fe) to be derived into oxides. In the cases of MIL-53(Fe)-400 and MIL-53(Fe)-500, lattice fringes with the spacing of 0.253 and 0.297 nm could be found, which were corresponded to the (311) and (220) crystalline facets of Fe₃O₄ (Fig. 2o and p)^{34,35}. The rhombic-shaped nanoparticles in MIL-53(Fe)-500 with higher crystallinity were distinct from the amorphous ones in MIL-53(Fe)-400. Diffraction rings consisting of unambiguous intense spots also confirmed the higher crystallinity of MIL-53(Fe)-500 in comparison with MIL-53(Fe)-400 (insets of Fig. 2o and p)^{35,36}. The energy dispersive spectroscopy (EDS) spectra revealed the existence of the Fe, C, and O elements (Supplementary Fig. 2). The high-angle annular dark-field scanning TEM (HAADF-STEM) and EDS mapping further showed a homogeneous dispersal of Fe, C, and O elements through the entire MIL-53(Fe), Q-MIL-53(Fe), MIL-53(Fe)-400, and MIL-53(Fe)-500 NPs (Fig. 2q–t). The morphology characterizations

confirmed the step-by-step derivation of the MIL-53(Fe) precursor, which resulted in a controlled decomposition, MOF skeleton collapse and emergence of iron oxides. The quasi-MOF feature of Q-MIL-53(Fe) could not be identified according to the morphology characterizations, which relies on further structural characterizations.

According to the TGA analysis depicted in Supplementary Fig. 3, MIL-53(Fe) started a decrease in mass before reaching 300 °C in N₂ atmosphere because of the release of solvent molecules from the pores. As the temperature increased over 350 °C, significant mass loss was observed in MIL-53(Fe), Q-MIL-53(Fe), and MIL-53(Fe)-400 due to structural collapse. Upon calcination at 600 °C, MIL-53(Fe), Q-MIL-53(Fe), MIL-53(Fe)-400, and MIL-53(Fe)-500 lost 78, 49, 27, and 13% of their initial weight, respectively. It was confirmed that higher calcination temperature in the synthesis procedure resulted in higher extent of structural collapse. The 49% weight loss of Q-MIL-53(Fe) after complete derivation demonstrated its partial deligandation when compared to 78% weight loss of MIL-53(Fe) and 27% weight loss of MIL-53(Fe)-400. The X-ray diffraction (XRD) pattern of MIL-53(Fe) exhibited characteristic peaks in accordance with those previously reported, implying that a highly crystalline structure was successfully formed (Supplementary Fig. 4)^{37,38}. The minor differences could be originated from the breathing effect of the MIL-53 scaffold, which facilitate the mass transport and access of the active sites^{39,40}. After calcination, distinct differences in the XRD patterns implied a gradual derivatization process with temperature increasing (Fig. 3a). The broadening of the diffractions around 5.0–10.0° from the MIL-53(Fe) thermalized at

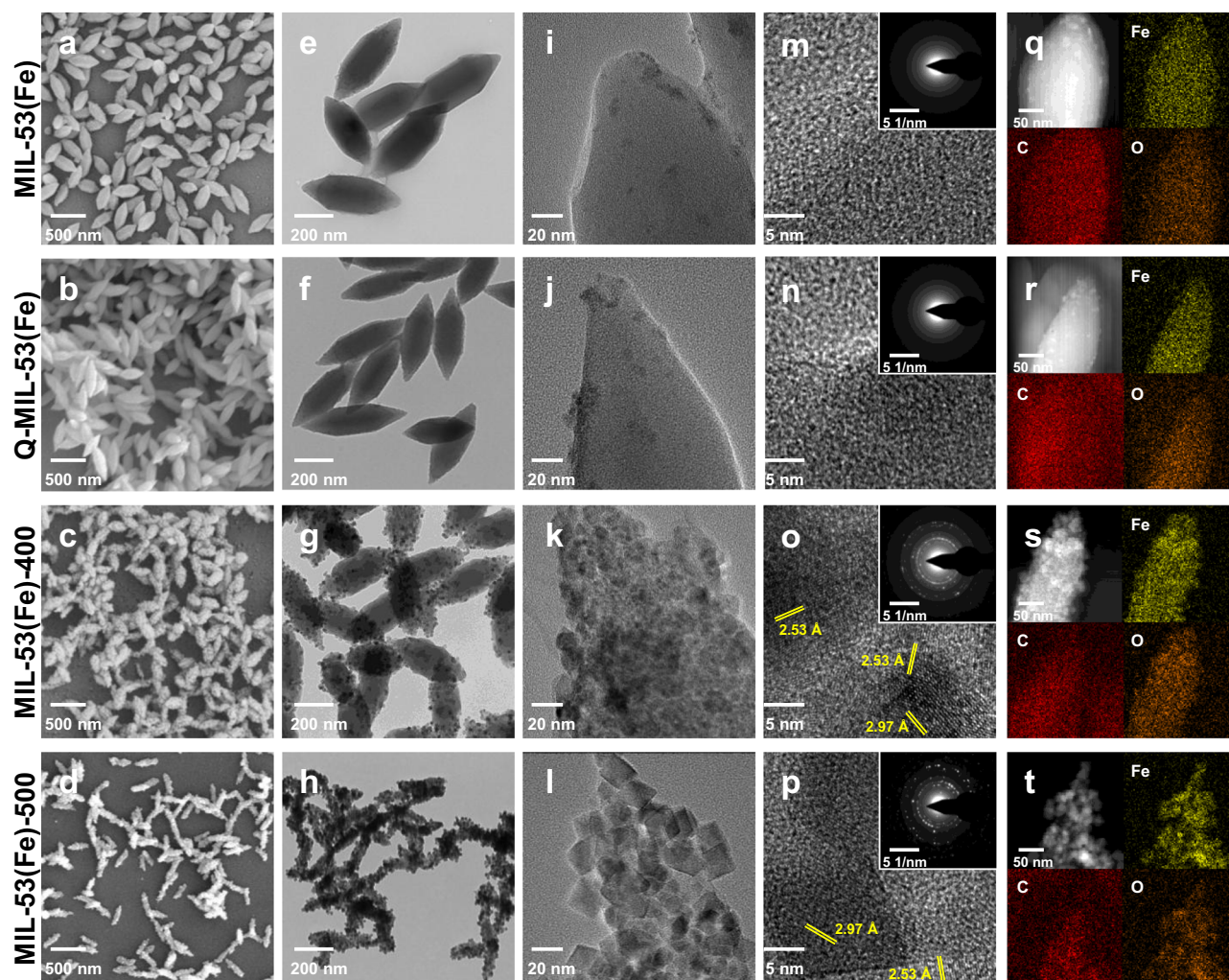


Fig. 2 | Morphological characterizations of MIL-53(Fe), Q-MIL-53(Fe), MIL-53(Fe)-400, and MIL-53(Fe)-500. a–d SEM images, e–h TEM images, i–l magnified TEM images, m–p HRTEM images (Inset: SAED images) and q–t HAADF-STEM

images and the corresponding EDS elemental mappings of MIL-53(Fe) (a,e,i,m,q), Q-MIL-53(Fe) (b,f,j,n,r), MIL-53(Fe)-400 (c,g,k,o,s), and MIL-53(Fe)-500 (d,h,l,p,t). All images are representative of three independent experimental replicates.

350 °C was observed, suggesting the incipient deligandation and decreased crystallinity of MIL-53(Fe)³⁰. However, diffraction peaks at 30.1, 35.4, and 43.0° corresponding to the (220), (311), and (400) facets of Fe₃O₄ (PDF#85-1436) were observed when the calcination temperature reached 400 °C. The remaining of MOF skeleton and the absence of resulting iron oxide are critical for the identification of quasi-MOF, which in this case verified the structure of Q-MIL-53(Fe)⁴¹. At even higher calcination temperature of 500 °C, the peaks around 10.0° disappeared and the diffraction peaks of Fe₃O₄ increased, indicating the complete collapse of MIL-53(Fe) and higher crystallinity of Fe₃O₄. The XRD results revealed temperature-dependent thermal transformation of the MOF, which is in accordance with the TEM and HRTEM images. Fourier transform infrared (FTIR) and Raman scanning were performed on MIL-53(Fe), Q-MIL-53(Fe), and MIL-53(Fe)-400/500 powders to evaluate the structural evolution of the MIL-53(Fe) (Fig. 3b and c). The FTIR spectra of MIL-53 show peaks at 1590 and 1392 cm⁻¹, which correspond to the vibrations of carboxyl groups, whereas the peak around 550 cm⁻¹ is assigned to the vibration of Fe–O in MIL-53(Fe)⁴². When pyrolyzed at 350 °C, it was observed that the intensity of the carboxylate bands slightly broadened, which suggested partial decomposition through the release of CO₂ from the ligand. It brought about the formation of accessible Fe–O sites^{40,43}. When the temperature attained 400 °C and CO₂ was further eliminated from the terephthalate ligand, more available Fe–O sites were attained on MIL-53(Fe). It

confirmed that Fe₃O₄ nanoparticles were formed within MIL-53(Fe)-400 in-situ⁴⁴. In Raman spectra the narrow peak of MIL-53(Fe) proved its high crystallinity. The sharp peak of MIL-53(Fe) was retained in the Q-MIL-53(Fe) and underwent a broadening trend, suggesting that partial decomposition and disrupted lattice of MIL-53(Fe). MIL-53(Fe)-400/500 exhibited two wide peaks with main frequencies at 1600 and 1340 cm⁻¹ corresponding to graphitic crystallite structures (G band) and disordered carbon components (D band), respectively. The Brunauer-Emmett-Teller (BET) surface area and total pore volume of Q-MIL-53(Fe) were comparable to those of MIL-53(Fe) and MIL-53(Fe)-400, confirming its intermediate structure (Supplementary Fig. 5). The enhanced surface area and total pore volume of MIL-53(Fe)-500 could be attributed to the totally transformation from MOF to amorphous carbon.

To further investigate the chemical environment of Fe, O and C ions in the four as-prepared materials, X-ray photoelectron spectroscopy (XPS) confirmed the presence and of Fe, O, and C elements, as indicated by the survey spectra (Supplementary Fig. 6). The results for MIL-53(Fe) showed that the peaks for Fe 2p_{3/2} and Fe 2p_{1/2} were located at 711.4 and 725.0 eV, respectively^{45,46}. Compared to MIL-53(Fe), the Fe 2p_{3/2} peaks of Q-MIL-53(Fe), MIL-53(Fe)-400, MIL-53(Fe)-500 shifted toward lower binding energy with the calcination temperature increasing, indicating the electron transfer from the coordinated O atom to the Fe ions (Fig. 3d)⁴⁷. The Fe 2p_{3/2}

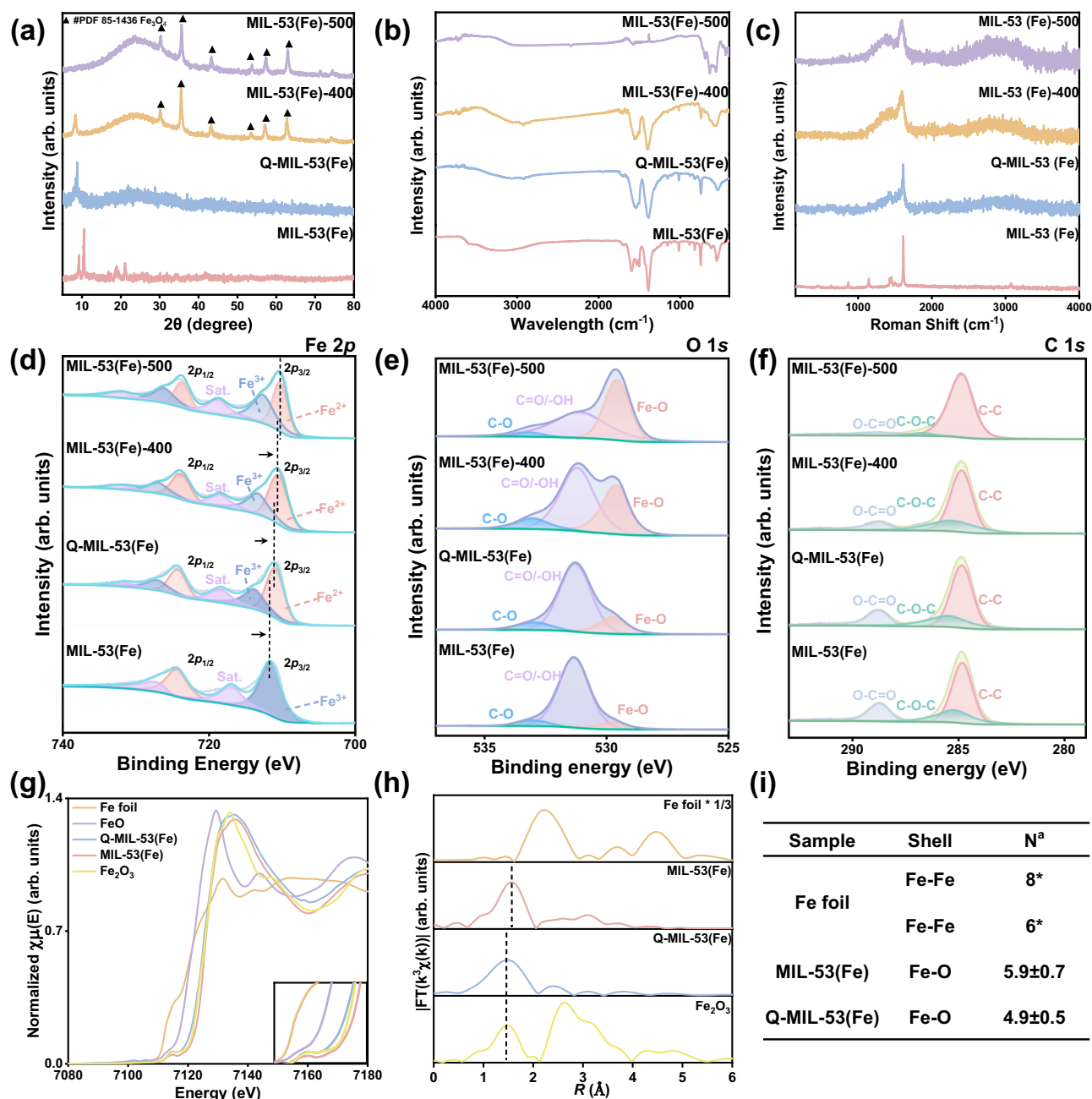


Fig. 3 | Structural characterizations of MIL-53(Fe), Q-MIL-53(Fe), MIL-53(Fe)-400, MIL-53(Fe)-500. **a** XRD patterns, **b** FT-IR spectra, **c** Raman spectra, and **d–f** high-resolution Fe 2p (**d**), O 1s (**e**), C 1s (**f**) for MIL-53(Fe), Q-MIL-53(Fe), MIL-53(Fe)-400, MIL-53(Fe)-500. **g**, **h** Normalized Fe K-edge XANES spectra (**g**) and

magnitude of k^3 -weighted Fourier transforms of the EXAFS spectra (**h**) of MIL-53(Fe), Q-MIL-53(Fe), FeO and Fe foil. **i** Fitting results of the coordination numbers of MIL-53(Fe) and Q-MIL-53(Fe). Source data are provided as a Source Data file.

peak of Q-MIL-53(Fe) can be assigned to 711.1 and 713.9 eV, corresponding to Fe^{2+} and Fe^{3+} , which also shifted in the spectra of MIL-53(Fe)-400/500⁴⁸. The ratio of $\text{Fe}^{2+}/\text{Fe}^{3+}$ maintained around 1:1 ignoring the calcination temperature varies which suggested the Fe reduction in all three derived samples. The high-resolution of O 1s spectra of MIL-53(Fe) NPs can be deconvoluted into three peaks, including 533.2 eV, 531.4 eV and 529.7 eV, corresponding to C–O bond, O=C/OH, and Fe–O bond, respectively^{45,49} (Fig. 3e). The proportion of Fe–O bond is increased with calcination temperature increasing, which also confirmed the emergence of iron oxides. The high-resolution spectra of C 1s in Fig. 3f are deconvoluted into three individual peaks, in accordance with C–C (284.6 eV), C–O (286.5 eV), and O–C=O (288.7 eV)^{50,51}. As the temperature of

calcination increases, the peaks of C=O and C–O become less dominating. The C=O peak almost disappeared in MIL-53(Fe)-500, attributing to that the terephthalic acid ligand decomposed with increasing temperature, and the ligand was completely disintegrated at 500 °C. The O 1s and C 1s spectra confirmed the deligandation of MIL-53(Fe) from partially to completely^{52,53}.

To further reveal the coordination environment and electronic structure of Q-MIL-53(Fe) in the derivation, XAS analysis was conducted. The X-ray absorption near edge structure (XANES) spectra at the Fe K-edge of Q-MIL-53(Fe) showed a lower absorption edge (E_0) than that of MIL-53(Fe), indicating partially reduction due to the deligandation, which was accordant with the binding energy shift in XPS analysis (Fig. 3g). The energy absorption threshold of Q-

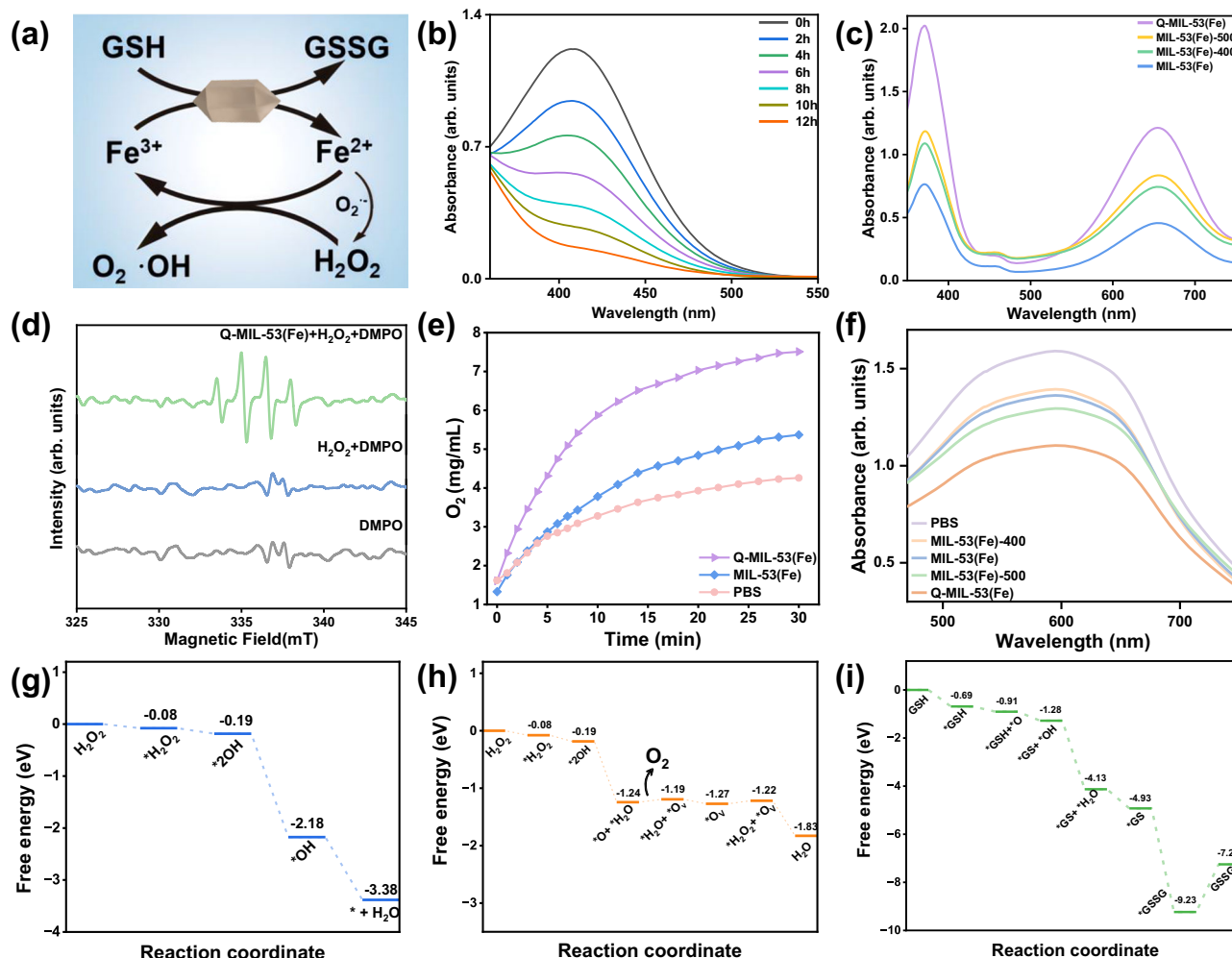


Fig. 4 | Multienzymatic activities and mechanisms. **a** Schematic illustration of the enzyme-like activity. **b** The GPX-like activity of Q-MIL-53(Fe) with different reaction time. **c** Peroxidase-like activities among different materials. **d** ESR spectra demonstrating $\cdot\text{OH}$ generation by Q-MIL-53(Fe) + H_2O_2 . **e** Time-dependence of O_2

production of H_2O_2 reacted with Q-MIL-53(Fe), MIL-53(Fe), and PBS solution. **f** Absorption spectra of the mixture of NBT with riboflavin and methionine in PBS solution or different materials. **g–i** Free energy diagrams of Q-MIL-53(Fe) in POD (**g**)/CAT (**h**)/GPX (**i**)-like activities. Source data are provided as a Source Data file.

MIL-53(Fe) is located between FeO and Fe_2O_3 , indicating that the valence of Fe is between +2 and +3 in Q-MIL-53(Fe). The coordination environment was then investigated by Fourier-transformed k3-weighted extended X-ray absorption fine structure (EXAFS) at the Fe K-edge (Fig. 3h). The EXAFS spectra of MIL-53(Fe) show main peak located at 1.56 Å which could be assigned to the Fe-O coordination bond. The peaks of Q-MIL-53(Fe) and Fe_2O_3 show main peaks at about 1.45 Å, coincidentally. The slightly lower R of the peaks of Q-MIL-53(Fe) verified that the Fe-O interaction was similar to the covalent bond in iron oxides, which was enhanced after the deligandation. Notably, the peaks of Fe-Fe interaction at 2.22 Å in Fe foil or at 2.64 Å for the second coordination sphere in Fe_2O_3 have not been detected in either MIL-53(Fe) or Q-MIL-53(Fe), confirming the atomically dispersed Fe without aggregation into iron or iron oxides NPs. EXAFS curve-fitting analysis in k and R spaces was performed to obtain the coordination configuration of Fe (Fig. 3i, Supplementary Fig. 7 and Supplementary Table 1). The Fe-O coordination numbers for MIL-53(Fe) and Q-MIL-53(Fe) were calculated to be 5.9 ± 0.7 and 4.9 ± 0.5 , respectively. The decreased coordination number of Q-MIL-53(Fe) contribute to the accessible catalytic sites and local valance variations of Fe. The result further validated the successful coordination configuration modifications of catalytic metal site via controlled deligandation strategy.

Multienzymatic performances and mechanisms

We further investigated the multienzyme-mimicking properties of Q-MIL-53(Fe) NPs after confirming its monodispersity and stability (Fig. 4a, Supplementary Fig. 8). GSH is an abundant endogenous antioxidant and can maintain the redox balance of cells to inhibit ROS-induced cell destruction⁵⁴. The effectiveness of treatments relying on ROS can be compromised due to elevated levels of GSH in cancer cells^{55–58}. Depletion of intracellular GSH is a pathway that destroys tumor cells, and GSH-depletion can enhance chemodynamic therapy (CDT), which induces ferroptosis and immune response^{59,60}. Then the ability of Q-MIL-53(Fe) for GSH depletion was investigated. The excessive amount of GSH was incubated with Q-MIL-53(Fe) NPs, and the remaining GSH was determined using 5,5'-dithiobis(2-nitrobenzoic acid) (DTNB), a specific indicator for sulfhydryl ($-\text{SH}$) groups, at various time intervals⁶¹. The absorbance at 412 nm, indicative of GSH concentration, showed a decline within a 12-hour period, suggesting complete depletion of GSH (Fig. 4b). The GSH consumptions of MIL-53(Fe) and MIL-53(Fe)-400/500 in the same circumstances were also analyzed (Supplementary Fig. 9). The findings demonstrated that Q-MIL-53(Fe) NPs were effective in depleting glutathione, whereas MIL-53(Fe) and MIL-53(Fe)-400/500 did not fully deplete GSH within the same time (Supplementary Fig. 10a). The GSH consumption is also validated to be promoted in the presence of H_2O_2 (Supplementary Fig. 10b).

Among the ROS family including $\cdot\text{OH}$, O_2^- , and $^1\text{O}_2$, $\cdot\text{OH}$ is commonly regarded as the most potent and harmful species formed during Fenton reaction for inducing CDT^{62,63}. To verify that Q-MIL-53(Fe) NPs can function as a Fenton-like agent, 3,3',5,5'-tetramethylbenzidine (TMB) was used in POD-like activity validation as the substrate for HRP in the presence of H_2O_2 ⁶⁴. According to the results in Fig. 4c, all groups showed absorption peaks of ox-TMB at 370 nm and 652 nm, confirming the POD-like activities of the as-prepared samples in the presence of H_2O_2 . Specifically, Q-MIL-53(Fe) displayed the greatest POD-like activity among the tested samples, providing solid evidence of its superior capability for generating $\cdot\text{OH}$ under room temperature (r.t.). With the decreased pH, there was a noticeable rise in the absorbance at 652 nm, indicating a higher production of $\cdot\text{OH}$ in an acidic buffer solution (pH 4.0), while this generation was limited in a neutral environment (pH 7.0) (Supplementary Figs. 11 and 12). The acidic-environment sensitivity endows the samples selectivity in acidic TME⁶⁵. To further quantitatively assess the catalytic capacity of Q-MIL-53(Fe) under r.t., steady-state catalytic kinetics of the reaction involving Q-MIL-53(Fe), TMB, and different concentrations of H_2O_2 (0.5, 1, 2.5, 5 and 10 mM) were investigated. The absorbance change at 652 nm in the reaction solution was continuously recorded over time. In the catalytic reaction, low K_m indicated the high affinity of Q-MIL-53(Fe) to the substrate. According to Supplementary Fig. 13, and Supplementary Table 2, the K_m and V_{\max} of Q-MIL-53(Fe) could be calculated as 1.08 mM and $1.117 \times 10^{-8} \text{ M s}^{-1}$, respectively. The V_{\max} of Q-MIL-53(Fe) exhibited a 3.5-fold, 2.6-fold and 2.4-fold improvements over MIL-53(Fe), MIL-53(Fe)-400, and MIL-53(Fe)-500 respectively. The K_m values of Q-MIL-53(Fe) were 1.8, 1.13, and 4.6-fold lower than MIL-53(Fe), MIL-53(Fe)-400, and MIL-53(Fe)-500. The K_m of Q-MIL-53(Fe) is lower than the reported derivatives of Fe-based MOF nanozymes, which reveals the efficient affinity enhancement of Q-MIL-53(Fe) with H_2O_2 (Supplementary Table 2). The POD-like catalytic performances of Q-MIL-53(Fe) was also confirmed to be comparable to that of HRP under 37 °C (Supplementary Fig. 14, Supplementary Table 2). Electron spin resonance (ESR) spectroscopy was exploited to validate the production of $\cdot\text{OH}$ species by using a spin trapper 5,5-dimethyl-1-pyrroline N-oxide (DMPO)^{66,67}. In contrast to the $\text{H}_2\text{O}_2 + \text{DMPO}$ and DMPO groups, which exhibited negligible peaks, the distinct quartet signal of $\cdot\text{OH}$ was observed in the presence of Q-MIL-53(Fe) NPs and H_2O_2 (Fig. 4d). The above outcomes prove that Q-MIL-53(Fe) possesses a TME-sensitive, and higher POD-like activity compared to the other three as-prepared nanomaterials.

Hypoxia can enhance the process of cancer cell metastasis and invasion, which contributes to treatment resistance⁶⁸. Q-MIL-53(Fe) NPs exhibited a stronger catalytic O_2 production performance than MIL-53(Fe) NPs in solutions with the same pH value, which is a characteristic of CAT-like activity⁶⁹ (Fig. 4e). Additional experiments confirmed that POD-like transformation of H_2O_2 was preferred in the intracellular environment, and the CAT-like transformation was preferred in the TME (Supplementary Fig. 15). Moreover, due to H_2O_2 concentration differentiation across the cell membrane, the POD-like catalysis of H_2O_2 was more significant and dominant in the treatment with tumor cells. SOD-like activity refers to the catalytic activity of transforming O_2^- into H_2O_2 and O_2 ⁷⁰. To evaluate the SOD-like activity of MIL-53(Fe) and its derivatives, nitro blue tetrazolium (NBT) as a probe to scavenge O_2^- . As shown in Fig. 4f, the absorbance peak decreased at 560 nm of Q-MIL-53(Fe) presented the most significant O_2^- scavenging ability among the four as-prepared samples. The POD/CAT/SOD-like catalytic performances of Q-MIL-53(Fe) have also been confirmed to be comparable to those of the natural enzymes, which indicated its significant activities (Supplementary Fig. 16).

To reveal the underlying mechanisms of the multienzymatic activities of Q-MIL-53(Fe), DFT calculations were performed. According to previous researches about the structure of the quasi MOF and the analysis of XRD, XPS and XAFS, the (110) facet of MIL-53 crystal

structure with Fe-O coordination number of 5 was selected as the active site and optimized (Supplementary Fig. 17a and b).

Regarding POD-like and CAT-like catalysis, computational studies revealed that H_2O_2 molecules readily interact with Fe atom, exhibiting an adsorption free energy of -0.08 eV (Fig. 4g and h). This interaction facilitates uniform H_2O_2 decomposition, generating both OH species and hydroxyl groups ($\cdot\text{OH}$) bound to Fe centers (Supplementary Figs 18 and 19). For POD-like catalysis, these surface-bound $\cdot\text{OH}$ species combine with protons to yield H_2O molecules on the Fe active sites in acidic environments, releasing free energies of 1.99 and 1.20 eV, respectively. The catalytic cycle completes when H_2O desorbs, restoring the initial Fe catalytic state and producing a significant decrease in Gibbs free energy (-3.38 eV, Supplementary Fig. 18). For CAT-like catalysis, adjacent $\cdot\text{OH}$ intermediates react with each other to produce $\cdot\text{O}$ and $\cdot\text{H}_2\text{O}$. An oxygen vacancy (Ov, 0.05 eV) is formed by releasing O_2 and H_2O molecules. Then the oxygen vacancy reacts with another H_2O_2 molecule to recover the catalyst site (Fig. 4h, Supplementary Fig. 19). In another reaction route, $\cdot\text{O}$ intermediate can participate in another H_2O_2 dissociation, forming $\cdot\text{OH}$ and $\cdot\text{OOH}$ with a free energy of 1.20 eV (Supplementary Fig. 20). Then the O_2 is formed with a Gibbs free energy decrease (-2.04 eV).

Analysis of GPX-mimicking behavior revealed spontaneous GSH adsorption onto Fe centers (Fig. 4i). With the assistance of water-dissolved O_2 , $\cdot\text{O}$ is formed for facilitating GSH dissociation (Supplementary Fig. 20). The reaction proceeds through two pathways: surface-bound $\cdot\text{GSH}$ and $\cdot\text{OH}$ interact to produce Fe-anchored $\cdot\text{GS}$ and H_2O , while $\cdot\text{GSH}$ can also react with $\cdot\text{O}$ to generate $\cdot\text{GS}$ and $\cdot\text{OH}$ species. Subsequently, these $\cdot\text{OH}$ intermediates combine with protons to release H_2O . The catalytic sequence results in GSSG formation through $\cdot\text{GS}$ dimerization. This process exhibits a substantial decrease in Gibbs free energy (-7.25 eV), confirming the GPX-mimicking capability (Supplementary Fig. 21). In the presence of H_2O_2 , the assistance of the generated $\cdot\text{OH}$ on the GSH oxidation is also studied. According to the calculated results in POD-like activity, the $\cdot\text{OH}$ (-2.18 eV) is generated on the active surface for further GSH adsorption to produce $\text{GSH} + \cdot\text{OH}$ (-2.94 eV) and $\cdot\text{GSH} + \cdot\text{OH}$ (-3.44 eV) (Supplementary Fig. 22). The free energy values of resulting $\cdot\text{GS}$ (-4.18 eV) and $\cdot\text{GSSG}$ (-8.48 eV) are comparable to that of the $\cdot\text{OH}$ -free route.

In vitro antitumor performances

To further evaluate the in vitro application potential of Q-MIL-53(Fe) NPs, the biocompatibility of Q-MIL-53(Fe) was investigated. It was evidenced that the iron-based Q-MIL-53(Fe) NPs showed negligible effects on the absorption/fluorescence-based cell experiments (Supplementary Fig. 23). The FITC-labelled Q-MIL-53(Fe) was observed to be internalized into 4T1 cells within 3 h according to the confocal laser scanning microscopy (CLSM) images, indicating its favorable cellular uptake (Supplementary Fig. 24). The CCK8 assay on L929 cells was undertaken to validate the low toxicity of Q-MIL-53(Fe) towards normal cell lines, demonstrating the desired cell compatibility and safety (Fig. 5a). The toxicity of Q-MIL-53(Fe) in breast cancer cells (4T1 and MCF-7 cells) was determined after 24 h incubation at a concentration of $100 \mu\text{g mL}^{-1}$. The cell viabilities of Q-MIL-53(Fe) for 4T1 and MCF-7 cells were 26.03% and 29.65%, respectively (Fig. 5b). The half-maximal inhibitory concentrations (IC_{50}) were calculated as 14.98 and $32.72 \mu\text{g mL}^{-1}$, respectively. While the IC_{50} of MIL-53(Fe) for 4T1 cells was $66.71 \mu\text{g mL}^{-1}$ (Supplementary Fig. 25). These results suggested the more efficient antitumor activity of Q-MIL-53(Fe) over MIL-53(Fe). As shown in the flow cytometric results for Annexin V-FITC and PI costained 4T1 cells after different treatments, Q-MIL-53(Fe) treatment resulted in higher early apoptosis (51.1 %) and late apoptosis (11.1 %) compared to that of the control group (2.09 % and 0 %) or MIL-53(Fe) (37.0 % and 4.42%) (Fig. 5c, Supplementary Fig. 26). To examine the ability of Q-MIL-53(Fe) and MIL-53(Fe) to produce intracellular ROS,

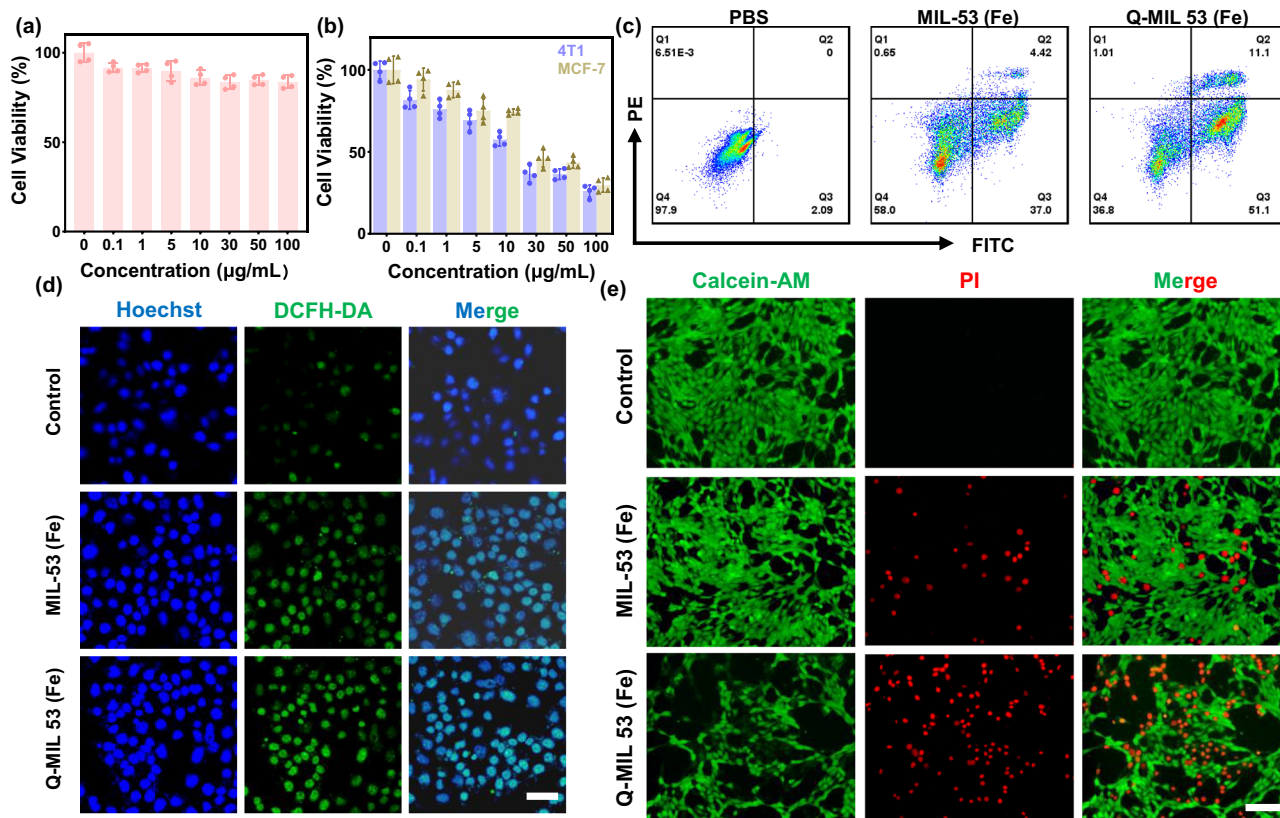


Fig. 5 | In vitro antitumor performances of MIL-53(Fe) and Q-MIL-53(Fe). **a** Cell viability of L929 cells incubated with diverse doses of Q-MIL-53(Fe). **b** Cell viability of breast cancer cells (4T1 and MCF-7 cells) treated using diverse doses of Q-MIL-53(Fe). **c** Flow cytometry of 4T1 cells after treatments with MIL-53(Fe) and Q-MIL-53(Fe) followed by staining with Annexin-V FITC and PI. **d** DCFH-DA stained 4T1 cells incubated with MIL-53(Fe) and Q-MIL-53(Fe). Scale bar = 40 μm . Images are

representative of three independent experimental replicates. **e** Live/dead staining of 4T1 cells after treatments with MIL-53(Fe) and Q-MIL-53(Fe) followed by Calcein-AM (green) and PI (red) staining. Scale bars = 200 μm . Images are representative of three independent experimental replicates. All data are presented as means \pm SD ($n = 4$ independent experiments for **a**, **b**). Source data are provided as a Source Data file.

2,7-Dichlorofluorescein diacetate (DCFH-DA) was applied to stain 4T1 cells. DCFH-DA reacts with ROS to produce 2,7-dichlorofluorescein (DCF), which exhibits green fluorescence⁷¹. According to Fig. 5d, Supplementary Figs. 27 and 28, there was a dim green fluorescence in the control groups. Both MIL-53(Fe) and Q-MIL-53(Fe) could lead to the ROS generation and the 4T1 cells treated with Q-MIL-53(Fe) showed brighter green fluorescence in comparison to the MIL-53(Fe) group, indicating that the Q-MIL-53(Fe) enhanced the production of ROS. The cells were also used for flow cytometry analysis which exhibited accordant ROS boosting results (Supplementary Fig. 29). The cells were costained with Calcein-AM and PI after being exposed to various experimental conditions to visually differentiate between living and dead cells. The control group experienced minimal cell damage, while the MIL-53(Fe) and Q-MIL-53(Fe) treated groups showed a significant presence of dead cells (Fig. 5e). More dead cells could be observed in the Q-MIL-53(Fe) treated cells. The results confirmed the Q-MIL-53(Fe)-induced intracellular ROS generation and cytotoxicity, which exhibited enhanced in vitro antitumor efficiency.

Since mitochondria have a significant impact in ferroptosis, the mitochondrial function and structure were analyzed⁷². The assessment of mitochondrial damage involved tracking the alteration in membrane potential using JC-1 dye as a fluorescent indicator. JC-1 dye emits red fluorescence when accumulating in mitochondria with high membrane potential. It emits green fluorescence if mitochondrial membrane potential (MMP) is under decrease. The cells treated with Q-MIL-53(Fe) NPs showed the least intense red fluorescence and the most intense green fluorescence compared to the control and MIL-53(Fe) treated groups (Fig. 6a, Supplementary Fig. 30). The flow

cytometry analysis also shows a notable reduction in the aggregates signals after the cells incubated with Q-MIL-53(Fe) in comparison with cells incubated with PBS or erastin, indicating evident MMP loss (Supplementary Fig. 31). Changes in mitochondrial morphology were studied using bio-TEM. It is revealed that Q-MIL-53(Fe) NPs mainly located in the mitochondria of 4T1 cells (Fig. 6b, Supplementary Fig. 32). Compared to the control group, the mitochondria of cells treated with Q-MIL-53(Fe) NPs manifested volume reduction via perimeter measurements, showing identical perimeter changes to those of mitochondria in cells treated with erastin (Supplementary Fig. 33)⁷². The mitochondrial morphological changes were supposed to be caused by Q-MIL-53(Fe) induced oxidative stress^{73,74}. Unlike the electron transport chain activity enhancement and mitochondrial hyperpolarization in ferroptosis induced by erastin, the MMP loss induced by Q-MIL-53(Fe) was supposed to be attributed to the mitochondrial subcellular distribution and subsequent oxidative damage towards mitochondrial membrane and functioning. Decreased GSH levels can inactivate GPX4 within cells and impede lipid repair mechanisms, ultimately resulting in ferroptosis⁷. Due to Q-MIL-53(Fe)'s capacity to deplete GSH, both the expression of GPX4 and its activity in 4T1 cells were significantly decreased following exposure to Q-MIL-53(Fe) (Fig. 6c, Supplementary Fig. 34). The inactivation of GPX4 and the overproduction of $\cdot\text{OH}$ can result in the accumulation of LPO, which is a significant indicator of ferroptosis⁷. The results showed elevated LPO levels in cells treated with Q-MIL-53(Fe) (2.60 %) compared to the intact cell (0.27%) and that treated with MIL-53(Fe) (0.48 %) using flow cytometry (Fig. 6d). The ferroptosis/apoptosis synergistic cell death paths induced by Q-MIL-53(Fe) was further confirmed through the

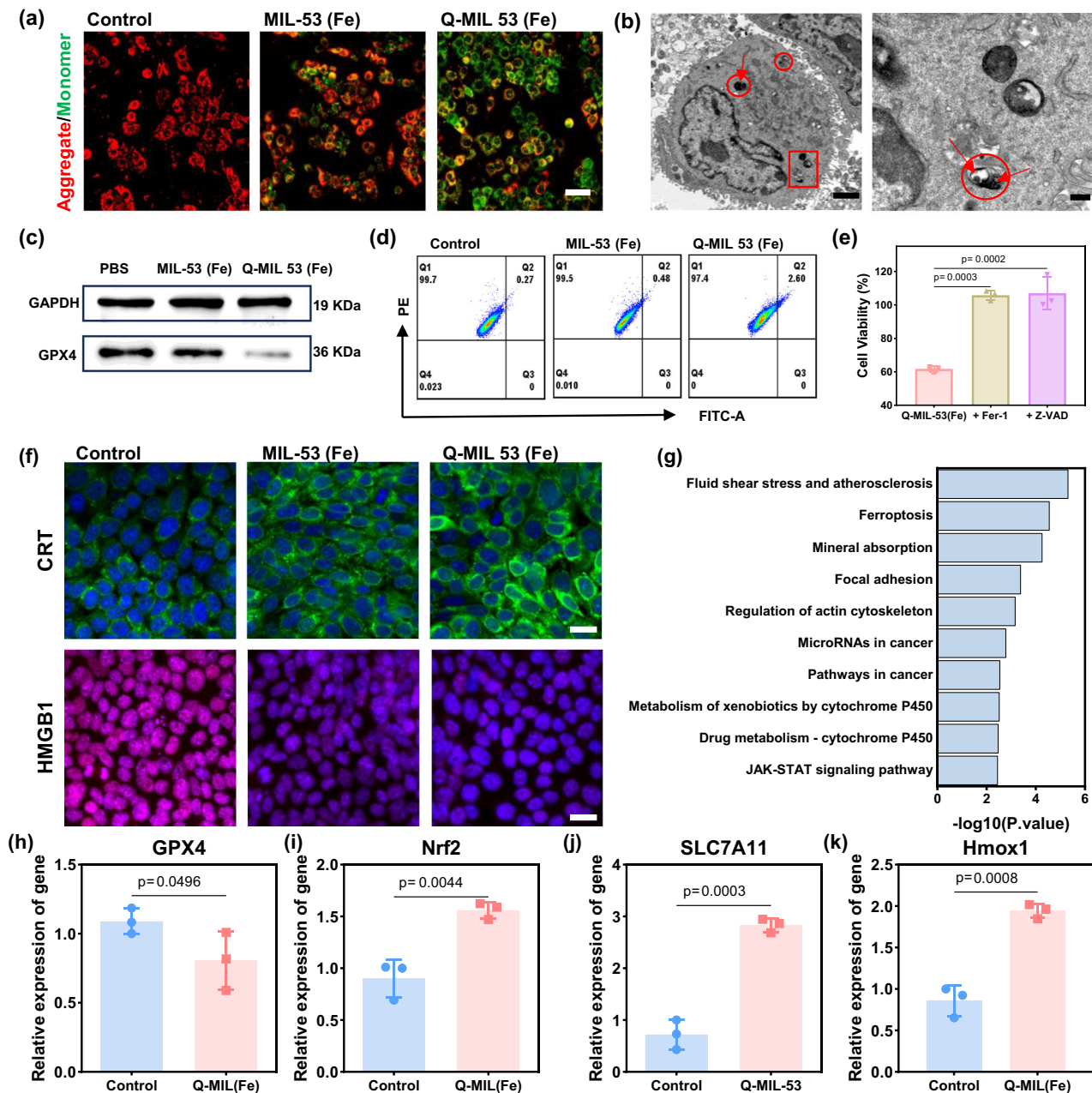


Fig. 6 | Induction of ferroptosis and ICD in 4T1 breast tumor cells by Q-MIL-53(Fe). **a** Confocal imaging of JC-1-stained 4T1 cells after different treatments with MIL-53(Fe) and Q-MIL-53(Fe). Images are representative of three independent experimental replicates. Scale bar = 20 μ m. **b** Bio-TEM images of 4T1 cells treated with Q-MIL-53(Fe). The right image is the enlarged view of the red squared area. Red arrow: internalized Q-MIL-53(Fe). Scale bar = 2 μ m and 500 nm, respectively ($n = 3$ independent experiments). **c** Protein expression levels of GPX4 were assessed in 4T1 cells subjected to MIL-53(Fe) and Q-MIL-53(Fe) treatment using WB detection. Images are representative of five independent experimental replicates with similar results. **d** Evaluation of intracellular LPO generation by flow cytometry. **e** Cell viability of 4T1 cells preincubated with Fer-1, Z-VAD followed by the treatments of Q-

MIL-53(Fe). All data are presented as means \pm SD ($n = 3$ independent experiments). The significance between each of the multiple groups was calculated using one-way ANOVA. **f** Confocal imaging of cellular protein expression levels of CRT and HMGB1 in 4T1 cell. Images are representative of three independent experimental replicates. Scale bar = 20 μ m. **g** KEGG enrichment analysis of the differentially expressed genes with |fold-change| > 1.5 and $p < 0.05$. **h–k** Relative expression of GPX4 (**h**), Nrf2(**i**), SLC7A11 (**j**) and Hmox1 (**k**). All data are presented as means \pm SD ($n = 3$ independent experiments for **h–k**). Significance between two groups was assessed by unpaired one-tailed Student's t-test (**h**) and unpaired two-tailed Student's t-test (**i–k**). Source data are provided as a Source Data file.

assessment of cell viability pretreated with ferroptosis inhibitor (ferrostatin-1) or apoptosis inhibitor (Z-VAD-FMK)⁷. The inhibitors pretreated 4T1 cells show significantly reduced Q-MIL-53(Fe)-induced death (Fig. 6e).

Chemotherapy could lead to the induction of ICD, resulting in the activation of an immune response against the tumor⁷⁵. The ICD-inducing effect was assessed by observing the presence of CRT and HMGB1 on the cell surface, as these are typical DAMPs for identifying

ICD^{10,11,75,76}. CRT can migrate from the endoplasmic reticulum to the cell surface when the cell is under stress. This movement acts as a signal for antigen-presenting cells to phagocytize dying tumor cells, which helps to stimulate the process of phagocytosis⁷⁷. The increase of CRT on the cell surface was observed in the 4T1 cells upon treatment with Q-MIL-53(Fe) (Fig. 6f, Supplementary Fig. 35). The migration of HMGB1 from the nucleus to the cytoplasm and extracellular space is another indicator to evaluate the ICD⁷⁸. The presence of Q-MIL-53(Fe)

NPs resulted in a notable reduction in the intracellular HMGB1 level, suggesting the translocation of HMGB1 from the nucleus (Fig. 6f, Supplementary Fig. 36). The results were further confirmed via flow cytometry (Supplementary Fig. 37). Moreover, considerable amounts of ATP were secreted into the extracellular milieu of 4T1 cells under the treatment of Q-MIL-53(Fe) NPs (Supplementary Fig. 38). The results indicated that Q-MIL-53(Fe) NPs treatment effectively enhanced the immunogenicity of cancer cells.

To further explore the impact of Q-MIL-53(Fe) on gene expression patterns, RNA-seq analysis was conducted on 4T1 cells subjected to Q-MIL-53(Fe) treatment. The mean sequencing coverages for the control and Q-MIL-53(Fe) treatment groups are 96.96% and 96.98% respectively (Supplementary Table 3). Compared with the control group of 4T1 cells, 73 upregulated and 123 downregulated differentially expressed genes (DEGs) ($|\log_2 \text{Fold change}| > 1$; $q \text{ value} < 0.05$), were identified in the Q-MIL-53(Fe) treated group. The DEGs are represented in a standard volcano plot (Supplementary Fig. 39a) and heatmap (Supplementary Fig. 39b). The DEGs could be found related to ferroptosis, mitochondria energetic metabolism, iron metabolism, and mitochondria-lipid metabolism (Supplementary Table 4). Among the DEGs, top 20 Gene Ontology (GO) terms of genes were identified with significant effects, including immune system process, immune process, defense response, iron ion transport, glutathione metabolic process (involved in biological process, BP), mitochondrion, mitochondrial inner membrane (involved in cellular component, CC), glutathione transferase activity, ferric iron binding, glutathione binding (involved in molecular function, MF), etc (Supplementary Fig. 40a–c). Kyoto Encyclopedia of Genes and Genomes (KEGG) enrichment analysis suggested that ferroptosis, glutathione metabolism pathways were identified (Fig. 6g, Supplementary Fig. 41d). Quantitative real-time polymerase chain reaction (qRT-PCR) was further performed, validating the downregulation of GPX4 and inducement of ferroptosis (Fig. 6h). Moreover, the regulation of Nrf2 (Nuclear factor erythroid 2 related factor 2, also known as NFE2L2) was investigated which contributes to redox balance maintenance and target genes regulation in iron homeostasis^{79,80}. Nrf2 might acts as either an anti- or pro-ferroptotic role depending on the pathological context⁸¹. Due to the ROS generation via Q-MIL-53(Fe) NPs catalyzing and its subsequent oxidative stress, Nrf2 and one of its downstream targets SLC7A11 (Solute Carrier Family 7 Member 11, also named as xCT) revealed upregulations which could be attributed to the cellular stress response against oxidative stress damages (Fig. 6i, j)⁸². Pharmacological agents such as erastin is reported as selective inhibitor of system x_c^- and cystine–glutamate exchange. It can cause the downregulation of SLC7A11 for preventing transmembrane transport of cystine and GSH production, thus favoring ferroptosis^{83,84}. However, in this case, the antioxidant effect via activation of Nrf2/SLC7A11 would not neutralize the LPO accumulation caused by intracellular GSH consumption and GPX4 downregulation of Q-MIL-53(Fe) NPs treatment. Moreover, heme-oxygenase 1 (Hmox1) was observed with a significant upregulation which was reported to be induced via Nrf2 activation (Fig. 6k)⁸⁵. Upregulation of Hmox1 is able to cause free iron release via heme degradation which accumulates in mitochondria and triggers lipid peroxidation⁸⁶. Thus, the activation of Nrf2, SLC7A11, Hmox1 combined contribute to the LPO accumulation and ferroptosis activation. The results suggest a potential modulation of cellular enzymatic pathways via Q-MIL-53(Fe) treatment, influencing cellular processes or responses.

In vivo therapeutic effect

The therapeutic efficacy of Q-MIL-53(Fe) was systematically assessed in vivo using Balb/c mice bearing 4T1 tumors, as depicted in Fig. 7a. The mice were randomly assigned into three groups of five each, labeled as the saline, MIL-53(Fe), and Q-MIL-53(Fe) groups followed by five intravenous (i.v.) injections. Over a period of 21 days, mice's weight

and tumor volume were monitored at three-day intervals while undergoing treatment. The tumor volume variations revealed a substantial inhibitory effect on tumor growth in both the MIL-53(Fe) and Q-MIL-53(Fe) groups compared to the saline group (Fig. 7b). The Q-MIL-53(Fe) treated cells showed better inhibition of tumor sizes, whose average volume was about 1/7 of MIL-53(Fe) and 1/22 of the saline group. The impact of each treatment on the mice's weight was negligible, pointing to the overall well-tolerance of all administered interventions (Supplementary Fig. 41). The tumors from all experimental groups were meticulously excised and weighed after treatment (Fig. 7c and d). The mean weights of tumors in the saline, MIL-53(Fe), and Q-MIL-53(Fe) groups were found to be 0.730, 0.228, and 0.023 g, respectively. These results demonstrated a marked inhibition of tumor growth induced by the administration of Q-MIL-53(Fe).

Hematoxylin and eosin (H&E) analysis was performed on tumor sections to assess the augmented therapeutic efficacy. The tumors treated with Q-MIL-53(Fe) had the most severe cell damage, as indicated by the substantial quantity of nuclear debris present. Immunohistochemical (IHC) staining for Ki-67 and immunofluorescence (IF) staining for TUNEL demonstrated the most significant reduction in the population of highly proliferative tumor cells and increased presence of apoptotic tumor cells of the Q-MIL-53(Fe) NPs treated group among the three administrations (Fig. 7e). IHC staining for GPX4 revealed the decrease of the positive signal, revealing its downregulation (Supplementary Fig. 42).

As evidenced by the in vitro analysis of the cellular CRT upregulation and HMGB1 release, the Q-MIL-53(Fe) induced ICD was also investigated ex vivo. The excised tumors were IF stained to analyze the expression of CRT and the discharge of HMGB1 in the tumor tissues. The Q-MIL-53(Fe) group exhibited markedly elevated levels of HMGB1 release and CRT exposure compared to the other groups (Fig. 7f), which are consistent with the in vitro analyses. The H&E staining of lungs revealed the populations and sizes of the metastatic nodule were decreased by MIL-53(Fe) to scattered level. Nodules could be barely found in the Q-MIL-53(Fe) treated group (Fig. 7g). The results revealed that Q-MIL-53(Fe) could eliminate the tumor metastasis in the lung area, indicating its anti-lung metastasis effect. Notably, the spleen of the mice treated with Q-MIL-53(Fe) was smaller compared to the other groups, indicating reduced immune suppression and promoting antitumor immunity^{87,88} (Supplementary Fig. 43a). These findings confirmed the better therapeutic benefits of the Q-MIL-53(Fe) over other treatments.

To confirm the biosafety of Q-MIL-53(Fe), histopathological and blood biochemistry analysis of major organs (heart, liver, spleen, lung, and kidney) was conducted after MIL-53(Fe) and Q-MIL-53(Fe) administrations. No obvious tissue damage was found (Supplementary Fig. 43b), which indicates the excellent biocompatibility of both MIL-53(Fe) and Q-MIL-53(Fe). Additionally, hemolysis and blood routine test analysis further confirmed that both the MIL-53(Fe) and Q-MIL-53(Fe) NPs had excellent blood compatibility and no significant long-term side effects (Supplementary Figs. 44 and 45). The results of Q-MIL-53(Fe) revealed that the tested common indexes are relieved almost within the normal ranges, preferable to that of MIL-53(Fe).

As antigen-presenting cells, DCs play a crucial role in initiating and regulating the innate and adaptive immunities which can lead to the significant stimulation of T cell proliferation. The induction of ferroptosis and ICD suggested its capability to activate tumor-specific immune responses. The ability of Q-MIL-53(Fe) to activate immune responses was further validated by monitoring DC maturation and T-cell infiltration (Fig. 8a). The percentage of mature DCs in tumor after Q-MIL-53(Fe) treatment was approximately 3.41-fold higher than that in the saline group (Fig. 8b, Supplementary Fig. 46a and 46b). DC maturation can activate the infiltration of T cells into the tumors. The CD3⁺ T cells in tumor after Q-MIL-53(Fe) treatment were increased from 1.69% to 4.6% (Supplementary Fig. 46c and d). Cytotoxic T lymphocytes (CTL, CD8⁺ T cells) along with helper T cells (CD4⁺ T cells)

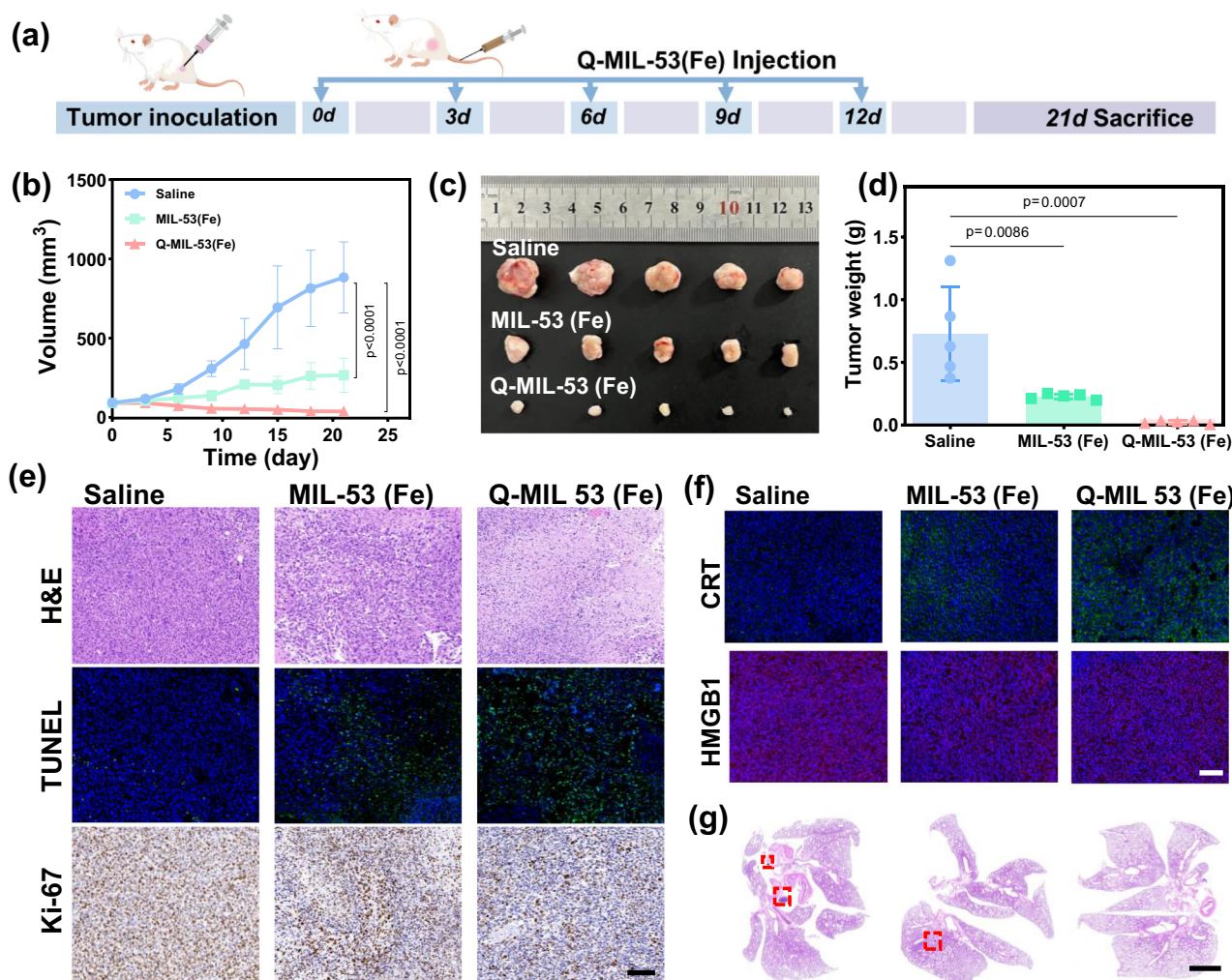


Fig. 7 | In vivo therapeutic effect. **a** Schematic illustration of experimental process of 4T1 tumor establishment and the therapeutic treatments. **b** The tumor growth curves of 4T1 tumor-bearing mice after indicated treatments. **c** Images of the harvested tumors. **d** The weight of tumors after treatment for i.v. injection groups. **e** H&E, TUNEL, and Ki-67 staining of tumor sections after 21 days of treatments. Scale bar = 100 μ m. **f** IF staining of tumor sections for CRT and HMGB1 expression.

Scale bar = 100 μ m. **g** H&E staining of the lung sections. Scale bar = 2000 μ m. Images are representative of three biologically independent mice (**e–g**). All data are presented as means \pm SD ($n = 5$ biologically independent animals for **b**, **d**) and the significance between each of the multiple groups was calculated using one-way ANOVA. Source data are provided as a Source Data file.

engage in vital functions in the direct combat toward cancer cells, which are essential for the regulation of adaptive immunities. CD4⁺ T cells and CD8⁺ T cells in CD3⁺ T cells displayed a distinct increase in the Q-MIL-53(Fe) groups from 64.5% to 78.9%, thereby revealing local immune response in the tumors (Fig. 8c, Supplementary Fig. 46e and 46f). Upon activation, T lymphocytes that infiltrate tumors release granules from their cytoplasm, with Granzyme B as a key component to eliminate malignant cells. Through the production of suppressive cytokines and dampening the activity of cytotoxic cells, FOXP3-expressing T cells compromise the immune response against tumors. The expression of Granzyme B and FOXP3 was investigated in tumors, which exhibited an obvious increase in the Q-MIL-53(Fe)-treated mice (Fig. 8d and e).

Recent studies have indicated that ferroptosis not only triggers ICD but also possesses the capability to amplify the efficacy of the tumor immune checkpoint inhibitor therapy⁸⁹. The synergistic anti-tumor efficacy of the combination of Q-MIL-53(Fe) and α PD-L1 was investigated. After i.v. injection of Q-MIL-53(Fe) into the 4T1 breast tumor bearing mice for two times, α PD-L1 was i.v. injected, which was schemed in Fig. 8f. The α PD-L1 group displayed a minor inhibition of tumor growth according to the recorded tumor volume and dissected

tumor which was due to the lack of PD-L1 expression in immune-excluded 4T1 breast tumors (Fig. 8g and h). The Q-MIL-53(Fe)/ α PD-L1 combination revealed a significant suppression of tumor growth whose averaged tumor weight was approximately 30% of the saline-treated mice, and 70% of the Q-MIL-53(Fe) treated mice (Fig. 8i). The body weights and organs of all the four groups showed negligible changes during the treatment, indicating the biosafety of the combination of Q-MIL-53(Fe)/ α PD-L1 (Fig. 8j and k). H&E staining of tumor revealed the most severe cell damage of the tumors treated with Q-MIL-53(Fe)/ α PD-L1 (Fig. 8l). In addition, the H&E staining of lung was also utilized to assess the in vivo anti-metastasis performance of Q-MIL-53(Fe) in combination with immune checkpoint inhibitor (Supplementary Fig. 47)^{90,91}. Q-MIL-53(Fe)/ α PD-L1 combination revealed the capacity to suppress tumor metastasis without metastatic nodules observed in the lungs. The synergizing with anti-PD-L1 antibody endow Q-MIL-53(Fe) immunotherapeutic capacity for significant suppression against primary tumors and lung metastasis.

In summary, fusiform nanozyme quasi MOF Q-MIL-53(Fe) derived from MIL-53(Fe) has been synthesized through the partial deligandation strategy. The Q-MIL-53(Fe) exhibited enhanced POD-, CAT-mimic activity and GSH depletion capacity which was the first quasi MOF for

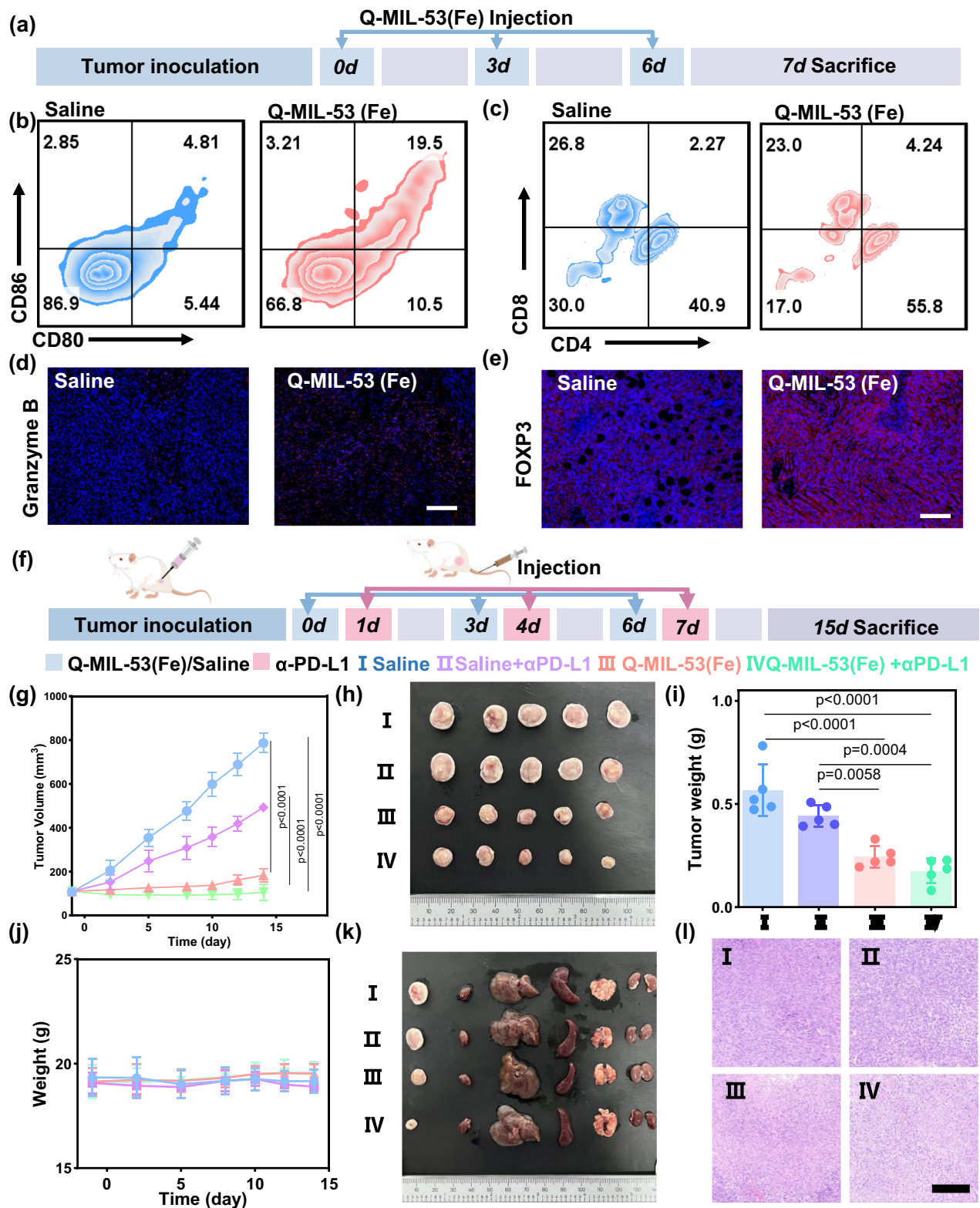


Fig. 8 | In vivo immunotherapeutic effects. **a** Schematic illustration of experimental process of in vivo antitumor immunity. **b** Flow cytometry analysis of mature DCs of tumors after saline and Q-MIL-53(Fe) treatment. **c** Flow cytometry analysis of CD4⁺ T cells and CD8⁺ T cells of tumors after saline and Q-MIL-53(Fe) treatment (the CD4⁺ T cells and CD8⁺ T cells were gated on CD3⁺ T cells). **d**, **e** IF staining of tumor sections for Granzyme B (**d**) and FOXP3 (**e**) expression. Images are representative of three biologically independent mice. Scale bar = 200 μ m. **f** Schematic illustration of the experimental process of in vivo immunotherapeutic effects. **g** The tumor growth curves of 4T1 tumor-bearing mice after indicated treatments. The

significance between each of the multiple groups was calculated using one-way ANOVA. **h** Images of the harvested tumors. **i** The recorded weight of tumors after different treatments. The significance between each of the multiple groups was calculated using one-way ANOVA. **j** The recorded weight of 4T1 tumor-bearing mice after indicated treatments. **k** Photographs of tumors and major organs (heart, liver, spleen, lung, and kidney). **l** H&E staining of the tumors sections. Scale bar = 100 μ m. Images are representative of three biologically independent mice. All data are presented as means \pm SD (n = 5 biologically independent animals for **g**, **i**, **j**). Source data are provided as a Source Data file.

antitumor application. The unique structural configuration of Fe active center was characterized via XAS analysis and its mechanisms of multienzymatic activities were also illustrated via DFT calculations. Q-MIL-53(Fe) showed excellent biocompatibility and demonstrated superior antitumor efficacy compared to MIL-53(Fe) *in vitro* and *in vivo*. The mechanism study revealed that Q-MIL-53(Fe) treatment induced LPO accumulation and activated ferroptosis via ROS boost, GSH depletion and mitochondrial dysfunction. It could also induce ICD and promote immune activation via DC maturation and T cell infiltration. Moreover, Q-MIL-53(Fe) treatment in combination of α PD-L1 exhibited synergistic effects for tumor inhibition, suggesting its potential to synergize with tumor immune checkpoint inhibitor therapy. This study provides the cancer immunotherapy potential of quasi MOF as a high-performance nanozyme platform. It also offers perspectives for the development of active MOF derived nanozymes.

Methods

Ethical regulations

All research complied with all relevant ethical regulations. All animal experiments *in vivo* are performed in strict accordance with the ARRIVE guidelines 2.0 and the Guidelines for the Care and Use of Laboratory Animals, and approved by the Animal Ethics Committee of Wenzhou University (No. WZU-2023-037). Female Balb/c mice (6–8 weeks old, ~20 g) were purchased from the Wenzhou University Laboratory Animal Center (Wenzhou, Zhejiang, China). The animal room temperature is 20–26 °C, warm humidity 40–70%, 12 hours of light and darkness alternate and all mice had free access to food and water. Female mice were opted in this study due to their more stable social behaviors, making them suitable for studies requiring long-term observation. To minimize animal discomfort, according to the Guideline of Assessment for Humane Endpoints in Animal Experiments (Certification and Accreditation Administration of the P. R. China, RB/T 173-2018), in general experiments, the tumor burden should not exceed 5% of the animal's normal body weight; in therapeutic experiments, it should not exceed 10% of the animal's body weight. In this study, no mice exceeded this criterion. At the end of the mouse experiments, mice were euthanized according to animal welfare standards (euthanasia of all animals was performed using isoflurane in small animal anesthetics).

Materials

$\text{FeCl}_3 \cdot 6\text{H}_2\text{O}$, terephthalic acid, 1,2-distearoyl-sn-glycero-3-phosphoethanolamine-N-[methoxy(polyethylene glycol)2000] (DSPE-PEG2000), N,N-Dimethylformamide, FeO , Fe_2O_3 , sodium hydroxide (NaOH), glutathione (GSH), 3, 3', 5, 5'-tetramethylbenzidine (TMB), riboflavin, L-methionine, NBT and H_2O_2 (30%) were purchased from local suppliers. Acetoxy-methylester of calcein (Calcein-AM), propidium iodide (PI) and 2',7'-dichlorodihydrofluorescein diacetate (DCFH-DA) were purchased from Beijing Solarbio Science & Technology Co. Ltd. JC-1 Mitochondrial Membrane Potential Detection Kit was purchased from Servicebio. All chemicals were used without any further purification.

Antibodies (anti-GAPDH, Beyotime, 1:1000; Goat anti-Rabbit IgG (H + L) Secondary Antibody, HRP, Beyotime, 1:1000; Goat anti-mouse IgG (H + L) Secondary Antibody, HRP, Beyotime, 1:1000; GPX4 Rabbit Polyclonal Antibody, Beyotime, 1:1000; PD-L1 Rabbit Monoclonal Antibody, Beyotime, 1:1000; Calreticulin Rabbit Monoclonal Antibody, Beyotime, 1:500; HMGB1 Rabbit Polyclonal Antibody, Beyotime, 1:200; IgG (H + L) (Alexa Fluor® 488-conjugated Donkey Anti-Goat IgG (H + L), Servicebio, 1:500; IgG (H + L), Cy3 conjugated Donkey Anti-Goat IgG (H + L), Servicebio, 1:500; FITC Anti-CD80 Rabbit pAb, Servicebio, 1:100; APC Anti-CD3 antibody, abcam, 1:100; PE Anti-CD86 antibody, abcam, 1:100; PE Anti-CD8 alpha antibody, abcam, 1:100; FITC Anti-CD4 antibody, abcam, 1:100.) were purchased from corresponding commercial sources with specific dilutions.

Instrumentation

X-ray diffraction (XRD) was measured on D8 Advance (Rigaku Corporation, Japan). Scanning electron microscope images were obtained on a SEM, Zeiss-Supra55. TEM images were obtained using Tecnai12 (Philips, Netherlands). Elemental mapping and high-angle annular dark-field scanning transmission electron microscope (HADF-STEM) images were performed on Tecnai G2 F30 transmission electron microscope. Fourier transform infrared spectroscopy was obtained from a Nicolet iS50 Fourier transform infrared spectrometer (Thermo Scientific, USA). Thermogravimetric analysis was performed on a TG 209 F3 instrument (Netzsch, Germany). X-ray photoelectron spectroscopy (XPS) was measured on a Thermo Scientific ESCALAB 250 apparatus, all peaks were calibrated with C1s peak binding energy at 284.6 eV for adventitious carbon. XAFS spectra at the Fe (7112 eV) K-edge were measured at the 1W1B beamline of the Beijing Synchrotron Radiation Facility (BSRF). Raman spectra were explored with a LabRAM UV-VIS-NIR 200 nm-2100 nm instrument. UV-vis absorption was monitored using a UV-vis spectrophotometer (UV-3600, Shimadzu). Confocal laser scanning microscopy (CLSM, Ti2, Nikon eclipse Co., Ltd, Japan). Flow cytometry was carried out on a flow cytometer (C6 Plus, BD Accuri Co., Ltd, Shanghai, China). WB images were achieved by a Tanon 5200 imaging analysis system (Tanon, Shanghai, China).

Synthesis of MIL-53(Fe)

MIL-53(Fe) can be synthesized by a hydrothermal method. $\text{FeCl}_3 \cdot 6\text{H}_2\text{O}$ (54 mg, 0.2 mmol) and terephthalic acid (H_2BDC , 33.2 mg, 0.2 mmol) were dissolved in N, N-dimethylacetamide (DMA, 12 mL). After stirring for 15 minutes at r.t., the mixture was sealed into a Teflon-lined stainless-steel hydrothermal reactor and reacted at 160 °C for 3 h. After the reaction, the mixture was cooled to r.t., and the precipitate was separated and washed three times with deionized water/ethanol.

Preparation of Q-MIL-53(Fe), MIL-53(Fe)-400, and MIL-53(Fe)-500

Q-MIL-53(Fe), MIL-53(Fe)-400, and MIL-53(Fe)-500 were prepared in traditional pyrolysis in a tube furnace under N_2 atmosphere at 350, 400, or 500 °C for 1 h with a ramp rate of 3 °C min^{-1} , followed by cooling at r.t. All the prepared samples were then mixed with DSPE-PEG-2000 in deionized water and kept under ultrasound for 20 min before use.

Enzyme-like activities

POD-like activity and kinetic assay. The POD-like activity of as-prepared MIL-53(Fe), Q-MIL-53(Fe), MIL-53(Fe)-400, and MIL-53(Fe)-500 was measured, respectively. Typically, H_2O_2 (20 μL , 10 mM) was added to 2 mL citrate buffer solution (pH = 4.0 or other pH values) containing as-prepared samples (30 $\mu\text{g mL}^{-1}$ or other concentrations) and TMB (200 μL , 1 mM). The reaction was kept for 15 min at r.t. Then the sample was analyzed using a UV-Vis spectrophotometer.

The steady-kinetic assays of the HRP and Q-MIL-53(Fe) (10 $\mu\text{g mL}^{-1}$) with TMB as the substrate were performed by adding TMB (1 mM) and different concentrations (5, 10, 25, 50, 100 μM) of H_2O_2 solutions. The absorbance of ox-TMB at 652 nm was measured by a UV-Vis spectrophotometer with different reaction times at 37 °C. Catalytic parameters were calculated from the Michaelis-Menten equation as follows:

$$v_0 = \frac{v_{\max}[\text{S}]}{K_m + [\text{S}]} \quad (1)$$

The steady-kinetic assays of the MIL-53(Fe) and its derived samples with TMB as the substrate were performed by adding TMB (1 mM) and different concentrations (0.1, 1, 2.5, 5, and 10 mM) of H_2O_2 solutions. The absorbance of ox-TMB at 652 nm was measured by a UV-Vis spectrophotometer with different reaction times. Catalytic parameters were calculated from Eq. (1).

GSH depletion measurement. The as-prepared samples ($30 \mu\text{g mL}^{-1}$) were uniformly dispersed in a PBS (pH 7.4) solution containing GSH (1 mM). It was allowed to react at 37°C for 12 h. After every 2 h, take 2 mL of the solution and mix it with DTNB (0.5 mM), and keep reacting for 15 min. Subsequently, the mixed solution was filtered using filter membrane (220 nm). The absorption of the solution was recorded at the wavelength from 350 to 550 nm.

CAT-like activity. The CAT-like activity of as-prepared MIL-53(Fe) and Q-MIL-53(Fe) were measured, respectively, by measuring the generated oxygen using a portable dissolved oxygen meter at r.t. In a typical assay, samples ($30 \mu\text{g mL}^{-1}$) were added to H_2O_2 (1 mM) in 5.0 mL PBS solutions (0.1 M , pH 7.4). The generated O_2 solubility (mg L^{-1}) was measured at different reaction times.

SOD-like activity. SOD-like activity of as-prepared MIL-53(Fe), Q-MIL-53(Fe), MIL-53(Fe)-400, and MIL-53(Fe)-500 was measured, respectively. The SOD activity of Q-MIL-53(Fe) was determined by the NBT reduction method. Riboflavin ($20 \mu\text{M}$), methionine (12.5 mM), NBT ($75 \mu\text{M}$), and as-prepared samples ($30 \mu\text{g mL}^{-1}$) were mixed in PBS solutions (pH 7.4) and treated with constant light irradiation for 15 min at r.t. The absorption of the solution was recorded at the wavelength from 350 to 550 nm. The absorption at 560 nm was denoted as A_0 and A_1 recorded before and after light irradiation, respectively. The absorption of control group recorded before and after light irradiation were A_c and A_{c0} , respectively. The SOD-like activities were calculated as follows: $\Delta\text{Abs} = (A_1 - A_0) / (A_c - A_{c0}) \times 100\%$.

ESR measurement. DMPO was elected as the nitrogen trapping agent to evaluate the hydroxyl radical generation. Sample solutions were obtained at r.t. by adding Q-MIL-53(Fe), H_2O_2 ($0, 10 \text{ mM}$), and DMPO (15 mg mL^{-1}) into 1 mL PBS solution (pH = 7.4). Then this sample solution was transferred to a quartz capillary tube and placed in the ESR cavity.

Computational methods. All the theoretical calculations were carried out with DFT method as implemented in the Vienna Ab Initio Simulation Package (VASP)⁹². The electron ion interaction was described with the projector augmented wave (PAW) method⁹³, while the electron exchange and correlation energy were solved within the generalized gradient approximation with the Perdew-Burke-Ernzerhof (PBE) exchange-correlation functional^{94,95}. DFT-D3 (D stands for dispersion) procedure was adopted to describe the van der Waals (vdW) interactions⁹⁶. The kinetic energy cutoff of plane wave was set to be 400 eV and the convergence criterion for the residual forces and total energies were set to be $0.03 \text{ eV } \text{\AA}^{-1}$ and 10^{-4} eV , respectively. A $3 \times 3 \times 1$ Monkhorst-Pack k-point grids was used to sample the Brillouin zone. The GGA + U relaxations have been carried out using $U = 7 \text{ eV}$ and $J = 1 \text{ eV}$ as Hubbard parameters on Fe 3 d states⁹⁷. A vacuum region of 24 \AA was created to ensure negligible interaction between layers.

The Gibbs free energy change (ΔG) for each elementary step was evaluated using the Computational Hydrogen Electrode (CHE) model⁹⁸, where the aqueous proton-electron pair's chemical potential is linked to half that of gaseous H . ΔG was calculated as: $\Delta G = \Delta E + \Delta\text{ZPE} - T\Delta S$. ΔE is the DFT-derived electronic energy difference between adsorbed reactants and products. ΔZPE and ΔS are zero-point energy and entropy corrections (adsorbed vs. gas phase) from vibrational frequency analysis at 298.15 K .

Cell culture. Mouse breast carcinoma cells (4T1) and NCTC clone 929 cells (L929), were cultured in DMEM medium containing 10% FBS and 1% antibiotics (penicillin-streptomycin, 10 U mL^{-1}). Human breast cancer cells (MCF-7) were cultured in RPMI-1640 medium containing 10% FBS and 1% antibiotics. All the cells were incubated at 37°C and 5% carbon dioxide (CO_2).

Intracellular anti-interference capacity. The DCFH-DA (DMSO, 1 mL, 1.0 mM) and NaOH (1 mL, 10 mM) were incubated for 30 min with stirring under 37°C . Then HCl ($10 \mu\text{L}$, 1 M) was added and stirred for 5 min to halt the hydrolysis reaction, and a DCFH solution was obtained. DCFH ($20 \mu\text{M}$) and Q-MIL-53(Fe) ($30 \mu\text{g mL}^{-1}$) were mixed in PBS solution (2 mL , pH 4) with or without H_2O_2 ($100 \mu\text{M}$), and the fluorescence spectra were recorded at 522 nm ($\lambda_{\text{ex}} = 495 \text{ nm}$). The DCFH or Q-MIL-53(Fe) solution alone was used as a control.

The 4T1 cells were seeded in a 96-well plate with 8×10^3 cells per well and incubated overnight. Then the cells were added with $100 \mu\text{L}$ DMEM and $10 \mu\text{L}$ CCK8 as the positive control. In the other groups, $100 \mu\text{L}$ DMEM and $10 \mu\text{L}$ CCK8 were added as the negative followed by addition of Q-MIL-53(Fe) with concentrations of 0.1, 1, 5, 10, 30, $50 \mu\text{g mL}^{-1}$, and incubation at 37°C for 2 h. The absorbance at 490 nm were recorded.

Cytotoxicity assay. In vitro cytotoxicity of the as-prepared samples towards L929, 4T1, and MCF-7 cells was determined by the CCK8 assay. Cells were seeded overnight in 96-well plates at a density of 8×10^3 per well. The medium was discarded and washed with PBS solutions. The cells were then incubated with different concentrations of MIL-53(Fe) and Q-MIL-53(Fe) ($0, 12.5, 25, 40, 50, 80, 100 \mu\text{g mL}^{-1}$) for further 24 h. The medium was then replaced with $100 \mu\text{L}$ fresh medium and $10 \mu\text{L}$ CCK8 solution was added to each well. The cells were then incubated for another 1 h. After incubation, the absorbance at 450 nm was measured using a microplate reader.

4T1 Cells co-incubation with inhibitors. Typically, 4T1 cells were seeded in 96-well plates at a density of 8×10^3 cells per well. After 12 h of cultivation, ferroptosis inhibitor (Ferrostatin-1, $10 \mu\text{M}$), caspase inhibitor (Z-VAD-FMK, $10 \mu\text{M}$) were added to the fresh medium for a further 2 h of cultivation. The 96-well medium was then discarded, washed with PBS solutions and incubated with Q-MIL-53(Fe) ($30 \mu\text{g mL}^{-1}$) for further 24 h. Cytotoxicity analysis was then performed.

Live/dead cell staining assay. 4T1 cells were seeded in confocal dishes at a density of 2×10^5 cells per dish and cultured at 37°C overnight. The previous medium was replaced with fresh medium containing MIL-53(Fe) ($30 \mu\text{g mL}^{-1}$) and Q-MIL-53(Fe) ($30 \mu\text{g mL}^{-1}$) for 12 h of co-incubation. The cells were then stained with Calcein-AM ($1 \mu\text{g mL}^{-1}$) and PI ($1 \mu\text{g mL}^{-1}$) for 30 min and observed under a CLSM.

The experiments with different concentrations were performed as above, and the different concentrations of Q-MIL-53(Fe) were incubated with the 4T1 cells.

Intracellular ROS level measurement. 4T1 cells were seeded on the confocal dish at a density of 1×10^6 cells overnight. The Q-MIL-53(Fe) ($30 \mu\text{g mL}^{-1}$) was incubated with cells for 6 h. After treatments, the cells were washed three times with PBS solutions. The cells were then incubated with DCFH-DA for 30 min, followed by washing three times with PBS solutions and nuclei with Hoechst 33342 labeling. The cells were observed under a CLSM at an excitation wavelength of 488 nm .

In a similar method, the cells were rinsed, digested, and collected after staining for flow cytometry.

Apoptosis assay. Cell apoptosis measurement against 4T1 cells was also performed using a flow cytometric assay with Annexin V-FITC and PI co-staining. Cells were incubated with as-prepared samples for 12 h, followed by washing with PBS solution. The cells were then stained with Annexin V-FITC/PI for 15 min and harvested for flow cytometric analysis.

Intracellular LPO detection. Intracellular LPO was detected using a C11-BODIPY 581/591 probe. Briefly, 3×10^6 cells were seeded on 6-well plates and cultured for 12 h. Cells were then washed with PBS solutions and co-incubated with Q-MIL-53(Fe) ($30 \mu\text{g mL}^{-1}$) in fresh medium for

another 12 h. Cells were then stained with C11-BODIPY 581/591 for 10 min and collected for flow cytometric analysis.

Mitochondrial membrane potential assay. For CLSM imaging, 4T1 cells were seeded in glass bottomed cell culture dish and incubated overnight. Then the cells were incubated with PBS solution or PBS solutions containing MIL-53(Fe) or Q-MIL-53(Fe) ($30 \mu\text{g mL}^{-1}$) for 12 h. Then the cells were washed 3 times and incubated with 1 mL of JC-1 staining working solution for 20 min. The cells were washed twice with PBS and observed on a CLSM.

For flow cytometry analysis, 4T1 cells were seeded in cell culture dish and incubated overnight. Then the cells were incubated with erastin ($10 \mu\text{M}$), MIL-53(Fe) and Q-MIL-53(Fe) ($30 \mu\text{g mL}^{-1}$) for 12 h. JC-1 solution was added and incubated for 20 min before the cells were collected for flow cytometry analysis.

TEM imaging of 4T1 cells. First, 5×10^7 cells were seeded onto a sterile dish (10 cm) and cultured for 24 h. The cells were then treated with Q-MIL-53(Fe) or erastin. After coincubation for 12 h, cells were collected and fixed in 2.5 % glutaraldehyde at 4°C overnight. After osmotic treatment, the samples were embedded and maintained at 70°C overnight. Thin sample sections were produced using an ultramicrotome and stained with 1 % uranyl acetate and 0.4 % lead citrate before TEM imaging.

Western Blotting analysis. Cells were seeded in dishes (10 cm) and incubated overnight. The supernatant was then removed and fresh media containing PBS solution, Q-MIL-53(Fe), and MIL-53(Fe) was added for co-incubation overnight. After treatment, 4T1 cells were collected and lysed in RIPA buffer with protease inhibitors for 30 min on ice. Protein concentrations were determined using BCA protein assay reagent. Proteins were separated on 15% sodium dodecyl sulfate-polyacrylamide gel electrophoresis (SDS-PAGE) and transferred to polyvinylidene difluoride (PVDF) membranes. Membranes were blocked with 5% non-fat milk and further incubated with the indicated primary antibodies GPX4 overnight at 4°C . The membranes were then incubated with Horse Radish Peroxidase (HRP)-conjugated secondary antibodies for 1 h at r.t. and scanned using an imaging analysis system.

Cellular immunofluorescence. The 4T1 cells were seeded into a confocal dish at a density of 5×10^5 cells per well. They were then incubated with PBS solutions, MIL-53(Fe), and Q-MIL-53(Fe) for 12 h, respectively. The 4T1 cells were washed three times with PBS solutions and fixed with 4% paraformaldehyde for 15 min. Subsequently, they were washed three times with PBS solutions and incubated with 0.1% Triton X-100 for 15 min at r.t. After removing the solution carefully, the cells were blocked with BSA for 30 minutes at r.t. Following three washes with PBS solutions, the cells were incubated with the antibody overnight at 4°C , respectively. The cells were washed three times with PBS solutions and then incubated with Cy3-conjugated or FITC-conjugated goat anti-rabbit secondary antibody for 30 minutes at r.t. Afterward, the nuclei were counterstained by incubating them with sealing agents that contained DAPI. Finally, the cells were analyzed via CLSM or flow cytometry.

Intracellular ATP measurement. The 4T1 cells were seeded into a 6-well plate at a density of 3×10^5 cells per well. They were then incubated with PBS solutions or PBS solutions containing MIL-53(Fe) and Q-MIL-53(Fe) ($30 \mu\text{g mL}^{-1}$) for 12 h, respectively. The 4T1 cells were washed with PBS solution for 3 times, digested and collected with Trypsin-EDTA solution for counting. Then use Ultrasonic crushing (ice bath, power 200 W), under 4°C for 1 min. After centrifuging at 121 g for 3 min, the ATP content test reagent was added to the supernatant for measurement with absorbance recorded at 450 nm.

In vivo antitumor assay. To establish a subcutaneous tumor model, 4T1 cells (1.5×10^7 cells) dispersed in PBS solutions were injected subcutaneously into the right side back of the mice. Tumor-bearing mice (tumor size $\approx 100 \text{ mm}^3$) were randomly assigned to three groups ($n = 5$ mice/group) for different treatments. Mice were i.v. injected with saline (group 1, 0.9% NaCl), MIL-53(Fe) (group 2, $30 \mu\text{g mL}^{-1}$), and Q-MIL-53(Fe) (group 3, $30 \mu\text{g mL}^{-1}$). Tumor volume and body weight were monitored during the 3 weeks of treatment. The tumor dimensions (maximum length L and maximum width W) were measured every other day with a caliper, and the tumor volume (V) was calculated as $V = L \times W^2/2 \text{ (mm}^3\text{)}$. The relative tumor volume was normalized to the initial size (V_0) before administration. The mice were sacrificed after 3 weeks, and the major organs (heart, liver, spleen, lung, and kidney) and tumors were harvested for immunohistology or immunofluorescence staining and analysis.

RNA isolation for sequencing and quantitative real-time PCR. The 4T1 cells were seeded in a 10 cm culture plate at a density of 3×10^5 cells per well and incubated overnight. Then the cells were treated with PBS solution or Q-MIL-53(Fe) PBS solutions ($30 \mu\text{g mL}^{-1}$) for 12 h. Total RNA was isolated and purified from the samples using TRIzol (Thermo-fisher, 15596018) according to the manufacturer's protocol. The quantity and purity of total RNA were then quality controlled using NanoDrop ND-1000 (NanoDrop, Wilmington, DE, USA), and RNA integrity was assessed using Bioanalyzer 2100 (Agilent, CA, USA). Samples satisfying the criteria of concentration $> 50 \text{ ng}/\mu\text{L}$, RIN value > 7.0 , and total RNA $> 1 \mu\text{g}$ were considered suitable. The RNA libraries were sequenced on the illumina Novaseq™ 6000 platform by LC Bio Technology CO., Ltd (Hangzhou, China) following standard procedures, with a sequencing mode of PE150. GO database released on 2021.05 (<http://geneontology.org>) and KEGG database Released on 2021.05 (<http://www.kegg.jp/kegg>) have been used for data analysis.

The 4T1 cells were seeded into 6 cm dishes at a density of 1×10^6 cells per dish and cultured overnight. Then, these cells were incubated with or without Q-MIL-53(Fe) ($30 \mu\text{g mL}^{-1}$) for 12 h. Subsequently, total RNA was extracted from cells using TRIzol. Then the concentration of RNA was detected and performed for PCR on a BIO-RAD CFX Connect Real-Time System by LC Bio Technology CO., Ltd (Hangzhou, China) following standard procedures with GAPDH as internal reference. The detailed procedure is as follows: The detailed qPCR procedure is as follows: The total qPCR reaction system was set to $10 \mu\text{L}$ with the following composition: $5 \mu\text{L}$ of $2 \times \text{SYBR}^\circledR$ Green Supermix (final concentration $1 \times$), $0.5 \mu\text{L}$ each of forward and reverse primers ($10 \mu\text{M}$, final concentration 200 nM), $1 \mu\text{L}$ of template cDNA, and RNase-free ddH_2O to make up the volume to $10 \mu\text{L}$. Gently mix the reaction system and aliquot it into RNase-free PCR tubes. Place the tubes into the real-time PCR instrument and perform the reaction under the following conditions: Pre-denaturation at 95°C for 3 min, followed by 39 cycles of denaturation at 95°C for 10 s and annealing at 60°C for 30 s, during which fluorescence signals are collected (FAM channel). After amplification, perform a melting curve analysis by increasing the temperature from 60°C to 95°C with 1°C increments, holding for 4 s at each step while collecting fluorescence signals. Upon completion, analyze the amplification curve for typical exponential growth and calculate Ct values, and check the melting curve for a single peak to confirm the specificity of the amplification.

In vivo antitumor immunity. To establish a subcutaneous tumor model, 4T1 cells (1.5×10^7 cells) suspended in PBS were injected subcutaneously into the right dorsal flank of the mice. Tumor-bearing mice (tumor volume $\approx 100 \text{ mm}^3$) were randomly assigned to two groups ($n = 5$ mice/group) for different treatments. The mice received i.v. injections of saline (group 1, 0.9% NaCl) or Q-MIL-53(Fe) (group 2, 5 mg/kg). Following three treatments, the mice were subjected to euthanasia via excessive gas anesthesia, and the

tumors were excised and placed in 75% alcohol solution for 15 min. The tumors were then rinsed with DMEM to remove debris and incubated with papain solution for digestion for 30 min. After digestion, the samples were centrifuged at 121 g for 5 min to remove the supernatant and washed twice with PBS. Subsequently, pancreatic enzyme digestion solution was added, and the samples were incubated at 37 °C with gentle shaking every 20 min. The digestion was terminated by adding serum, followed by centrifugation to remove the supernatant. The cells were washed with PBS, resuspended in DMEM, and stored at 4 °C. This process was repeated three times. After the final collection, the supernatant was removed by centrifugation, and a 1% BSA solution was added to prepare a single-cell suspension. The suspension was filtered through a 0.45 µm membrane, and 5×10^6 cells were collected and resuspended in PBS. Cells were then stained by anti-CD80-FITC, anti-CD86-PE, anti-CD8-PE, anti-CD4-FITC, and anti-CD3-APC antibodies and incubated for 30 min in the dark. Finally, flow cytometry analysis was performed.

Hemolysis test. Blood cells were collected from Balb/c mice and incubated with different amounts of Q-MIL-53(Fe) in tubes at 37 °C. After 60 min, the samples were centrifuged for the hemolysis analysis. The blood cells in PBS solution or distilled water without adding Q-MIL-53(Fe) were used as controls.

$$\text{hemolysis rate(\%)} = \frac{(\text{sample absorption} - \text{negative control absorption})}{(\text{positive control absorption} - \text{negative control absorption})} \times 100\%$$

In vivo immunotherapeutic effects. For the tumor inoculation, 4T1 cells (1.5×10^7) suspended in PBS were subcutaneously injected into the right flank of each female Balb/c mouse, respectively. The therapy started when the primary tumor volumes reached 100 mm³. The 4T1 tumor-bearing mice were divided into four groups randomly and administrated with 100 µL of saline, saline+αPD-L1, Q-MIL-53(Fe), and Q-MIL-53(Fe)+αPD-L1 (Q-MIL-53(Fe), 5 mg/kg, αPD-L1, 50 µg per mouse) through i.v. injection. Then the tumor volume and body weights of mice were recorded every two days. The tumor volume was calculated as the following formula: width² × length × 0.5. After 15 days, the mice were sacrificed. In addition, all the major organs (i.e., heart, liver, lung, and kidney) and tumors were collected with the examination by H&E staining.

Reporting summary

Further information on research design is available in the Nature Portfolio Reporting Summary linked to this article.

Data availability

The raw sequencing reads in RNA-seq are available on Genome Sequence Archive (GSA) on <https://ngdc.cncb.ac.cn/gsa/> via accession No. CRA018825. All data are available within the Article and Supplementary Files (Supplementary Information), or available from the corresponding authors upon request. Raw data are also available from Figshare (<https://doi.org/10.6084/m9.figshare.28358861.v1>). Source data are provided with this paper.

References

- Siegel, R. L., Miller, K. D., Wagle, N. S. & Jemal, A. Cancer statistics, 2023. *CA Cancer J. Clin.* **73**, 17–48 (2023).
- Siegel, R. L., Miller, K. D., Fuchs, H. E. & Jemal, A. Cancer statistics, 2022. *CA Cancer J. Clin.* **72**, 7–33 (2022).
- Wang, X., Yang, L., Chen, Z. & Shin, D. M. Application of nanotechnology in cancer therapy and imaging. *CA Cancer J. Clin.* **58**, 97–110 (2008).
- Waks, A. G. & Winer, E. P. Breast cancer treatment: a review. *JAMA* **321**, 288–300 (2019).
- Cheng, Z., Li, M., Dey, R. & Chen, Y. Nanomaterials for cancer therapy: current progress and perspectives. *J. Hematol. Oncol.* **14**, 85 (2021).
- Dixon, S. J. et al. Ferroptosis: an iron-dependent form of non-apoptotic cell death. *Cell* **149**, 1060–1072 (2012).
- Stockwell, B. R. et al. Ferroptosis: a regulated cell death nexus linking metabolism, redox biology, and disease. *Cell* **171**, 273–285 (2017).
- Stockwell, B. R. Ferroptosis turns 10: emerging mechanisms, physiological functions, and therapeutic applications. *Cell* **185**, 2401–2421 (2022).
- Jiang, X., Stockwell, B. R. & Conrad, M. Ferroptosis: mechanisms, biology and role in disease. *Nat. Rev. Mol. Cell. Biol.* **22**, 266–282 (2021).
- Krysko, D. V. et al. Immunogenic cell death and DAMPs in cancer therapy. *Nat. Rev. Cancer* **12**, 860–875 (2012).
- Galluzzi, L., Buqué, A., Kepp, O., Zitvogel, L. & Kroemer, G. Immunogenic cell death in cancer and infectious disease. *Nat. Rev. Immunol.* **17**, 97–111 (2017).
- Kroemer, G., Galassi, C., Zitvogel, L. & Galluzzi, L. Immunogenic cell stress and death. *Nat. Immunol.* **23**, 487–500 (2022).
- Xu, S., Min, J. & Wang, F. Ferroptosis: an emerging player in immune cells. *Sci. Bull.* **66**, 2257–2260 (2021).
- Wei, H. et al. Nanozymes: A clear definition with fuzzy edges. *Nano Today* **40**, 101269 (2021).
- Liang, M. & Yan, X. Nanozymes: from new concepts, mechanisms, and standards to applications. *Acc. Chem. Res.* **52**, 2190–2200 (2019).
- Huang, X. et al. Advances in metal-organic framework-based nanozymes and their applications. *Coord. Chem. Rev.* **449**, 214216 (2021).
- Gao, L. et al. Intrinsic peroxidase-like activity of ferromagnetic nanoparticles. *Nat. Nanotechnol.* **2**, 577–583 (2007).
- Wu, J. et al. Ligand-dependent activity engineering of glutathione peroxidase-mimicking MIL-47(V) metal-organic framework nanozyme for therapy. *Angew. Chem. Int. Ed.* **60**, 1227–1234 (2021).
- Chen, Y. et al. A manganese-based metal-organic framework as a cold-adapted nanozyme. *Adv. Mater.* **36**, e2206421 (2022).
- Zheng, S. et al. Dual-ligand and hard-soft-acid-base strategies to optimize metal-organic framework nanocrystals for stable electrochemical cycling performance. *Nat. Sci. Rev.* **9**, nwab197 (2022).
- Sun, Y. et al. Synergistic effect of oxygen vacancy and high porosity of nano MIL-125(Ti) for enhanced photocatalytic nitrogen fixation. *Angew. Chem. Int. Ed.* **136**, e202316973 (2024).
- Jiang, W. et al. Chiral metal-organic frameworks incorporating nanozymes as neuroinflammation inhibitors for managing Parkinson's disease. *Nat. Commun.* **14**, 8137 (2023).
- Zeng, L. et al. A MOF-based potent ferroptosis inducer for enhanced radiotherapy of triple negative breast cancer. *ACS Nano* **17**, 13195–13210 (2023).
- Zhang, H. et al. A versatile prodrug strategy to in situ encapsulate drugs in MOF nanocarriers: a case of cytarabine-IR820 prodrug encapsulated ZIF-8 toward chemo-photothermal therapy. *Adv. Funct. Mater.* **28**, e1802830 (2018).
- Zhao, X. et al. Preparation of photocatalytic and antibacterial MOF nanozyme used for infected diabetic wound healing. *ACS Appl. Mater. Inter.* **14**, 18194–18208 (2022).
- Yang, Y. et al. Platinum-carbon-integrated nanozymes for enhanced tumor photodynamic and photothermal therapy. *Nanoscale* **12**, 13548–13557 (2020).
- Chen, Q. et al. MOF-derived Co₃O₄@Co-Fe oxide double-shelled nanocages as multi-functional specific peroxidase-like nanozyme catalysts for chemo/biosensing and dye degradation. *Chem. Eng. J.* **395**, 125130 (2020).

28. Peng, Y. et al. Applications of metal–organic framework-derived N, P, S doped materials in electrochemical energy conversion and storage. *Coord. Chem. Rev.* **466**, 214602 (2022).
29. Xu, B. et al. A bioinspired five-coordinated single-atom iron nanozyme for tumor catalytic therapy. *Adv. Mater.* **34**, e2107088 (2022).
30. Tsumori, N. et al. Quasi-MOF: exposing inorganic nodes to guest metal nanoparticles for drastically enhanced catalytic activity. *Chem* **4**, 845–856 (2018).
31. Chen, L., Tsumori, N. & Xu, Q. Quasi-MOF-immobilized metal nanoparticles for synergistic catalysis. *Sci. China Chem.* **63**, 1601–1607 (2020).
32. Zhu, R. et al. Quasi-ZIF-67 for boosted oxygen evolution reaction catalytic activity via a low temperature calcination. *ACS Appl. Mater. Inter.* **12**, 25037–25041 (2020).
33. Cheng, Y., Xiao, X., Guo, X., Yao, H. & Pang, H. Synthesis of “Quasi-Ce-MOF” electrocatalysts for enhanced urea oxidation reaction performance. *ACS Sustain. Chem. Eng.* **8**, 8675–8680 (2020).
34. Luo, D. et al. Design of quasi-MOF nanospheres as a dynamic electrocatalyst toward accelerated sulfur reduction reaction for high-performance lithium-sulfur batteries. *Adv. Mater.* **34**, e2105541 (2022).
35. Yang, C. et al. Electrochemically reconstructed Cu-FeOOH/Fe₃O₄ catalyst for efficient hydrogen evolution in alkaline media. *Adv. Energy Mater.* **12**, e2200077 (2022).
36. Zhang, Y., Zhang, B.-T., Teng, Y., Zhao, J. & Sun, X. Heterogeneous activation of persulfate by carbon nanofiber supported Fe₃O₄@carbon composites for efficient ibuprofen degradation. *J. Hazard. Mater.* **401**, 123428 (2021).
37. Millange, F. et al. Selective sorption of organic molecules by the flexible porous hybrid metal-organic framework MIL-53(Fe) controlled by various host-guest interactions. *Chem. Mater.* **22**, 4237–4245 (2010).
38. Cheng, X., Zhou, X., Zheng, Z. & Kuang, Q. Construct efficient substrate transport and catalytic sub-nanochannels in metal-organic framework-based nanozymes for boosting peroxidase-like catalytic activity. *Chem. Eng. J.* **430**, 133079 (2022).
39. Serre, C. et al. Very Large breathing effect in the first nanoporous chromium(III)-based solids: MIL-53 or Cr^{III}(OH){O₂C–C₆H₄–CO₂}·{HO₂C–C₆H₄–CO₂}_x·H₂O_y. *J. Am. Chem. Soc.* **124**, 13519–13526 (2002).
40. Devic, T. et al. Functionalization in flexible porous solids: effects on the pore opening and the host–guest interactions. *J. Am. Chem. Soc.* **132**, 1127–1136 (2010).
41. Bagheri, M. & Masoomi, M. Y. Quasi-Metal Organic Frameworks: preparation, applications and future perspectives. *Coord. Chem. Rev.* **468**, 214643 (2022).
42. Ye, Z., Padilla, J. A., Xuriguera, E., Brillas, E. & Sirés, I. Magnetic MIL(Fe)-type MOF-derived N-doped nano-ZVI@C rods as heterogeneous catalyst for the electro-Fenton degradation of gemfibrozil in a complex aqueous matrix. *Appl. Catal. B* **266**, 118604 (2020).
43. Ai, L., Zhang, C., Li, L. & Jiang, J. Iron terephthalate metal-organic framework: Revealing the effective activation of hydrogen peroxide for the degradation of organic dye under visible light irradiation. *Appl. Catal. B* **148–149**, 191–200 (2014).
44. Liu, K. et al. Multiphase porous electrochemical catalysts derived from iron-Based Metal-Organic Framework compounds. *Environ. Sci. Technol.* **53**, 6474–6482 (2019).
45. Hua, B. et al. The excellence of both worlds: developing effective double perovskite oxide catalyst of oxygen reduction reaction for room and elevated temperature applications. *Adv. Funct. Mater.* **26**, 4106–4112 (2016).
46. Yang, Y. et al. Highly active trimetallic NiFeCr layered double hydroxide electrocatalysts for oxygen evolution reaction. *Adv. Energy Mater.* **8**, 1703189 (2018).
47. Qiu, Z. et al. 2D MOF-assisted pyrolysis-displacement-alloying synthesis of high-entropy alloy nanoparticles library for efficient electrocatalytic hydrogen oxidation. *Angew. Chem. Int. Ed.* **62**, e202306881 (2023).
48. Cheng, M. et al. Prussian blue analogue derived magnetic Cu-Fe oxide as a recyclable photo-Fenton catalyst for the efficient removal of sulfamethazine at near neutral pH values. *Chem. Eng. J.* **362**, 865–876 (2019).
49. Tang, L. et al. High configuration entropy activated lattice oxygen for O₂ formation on perovskite electrocatalyst. *Adv. Funct. Mater.* **32**, 2112157 (2022).
50. Wu, Q. et al. Peculiar synergetic effect of γ-Fe₂O₃ nanoparticles and graphene oxide on MIL-53 (Fe) for boosting photocatalysis. *Chem. Eng. J.* **390**, 124615 (2020).
51. Hu, C., Hu, X., Li, R. & Xing, Y. MOF derived ZnO/C nanocomposite with enhanced adsorption capacity and photocatalytic performance under sunlight. *J. Hazard. Mater.* **385**, 121599 (2020).
52. Shen, X. et al. Synergistic modulation at atomically dispersed Fe/Au interface for selective CO₂ electroreduction. *Nano Lett.* **21**, 686–692 (2021).
53. Jin, Z. et al. Understanding the inter-site distance effect in single-atom catalysts for oxygen electroreduction. *Nat. Catal.* **4**, 615–622 (2021).
54. Feng, L. et al. An ultrasmall SnFe₂O₄ nanozyme with endogenous oxygen generation and glutathione depletion for synergistic cancer therapy. *Adv. Funct. Mater.* **31**, 2006216 (2021).
55. Li, Y. et al. Self-initiated nano-micelles mediated covalent modification of mRNA for labeling and treatment of tumors. *Angew. Chem. Int. Ed.* **63**, e202411598 (2024).
56. Yin, J. et al. Cyanine-based fluorescent probe for highly selective detection of glutathione in cell cultures and live mouse tissues. *J. Am. Chem. Soc.* **136**, 5351–5358 (2014).
57. Lin, L. et al. Simultaneous Fenton-like ion delivery and glutathione depletion by MnO₂-based nanoagent to enhance chemodynamic therapy. *Angew. Chem. Int. Ed.* **57**, 4902–4906 (2018).
58. An, J. et al. A pH/ultrasound dual-response biomimetic nanoplat-form for nitric oxide gas-sonodynamic combined therapy and repeated ultrasound for relieving hypoxia. *Biomaterials* **230**, 119636 (2020).
59. Sun, Y., Zheng, Y., Wang, C. & Liu, Y. Glutathione depletion induces ferroptosis, autophagy, and premature cell senescence in retinal pigment epithelial cells. *Cell Death Dis.* **9**, 753 (2018).
60. Lv, M. et al. Evoking ferroptosis by synergistic enhancement of a cyclopentadienyl iridium-betulin immune agonist. *Angew. Chem. Int. Ed.* **62**, e202312897 (2023).
61. Ma, Y. et al. Biodegradable metal-organic-framework-gated organosilica for tumor-microenvironment-unlocked glutathione-depletion-enhanced synergistic therapy. *Adv. Mater.* **34**, 2107560 (2022).
62. Liu, Y. et al. One-dimensional Fe₂P acts as a fenton agent in response to NIR II light and ultrasound for deep tumor synergetic theranostics. *Angew. Chem. Int. Ed.* **58**, 2407–2412 (2019).
63. Zhang, Y. et al. Mild photothermal treatment sensitized immune checkpoint blockade therapy based on ATP-exhausted nanoenzymes. *Chem. Eng. J.* **474**, 145677 (2023).
64. An, J. et al. ROS-augmented and tumor-microenvironment responsive biodegradable nanoplat-form for enhancing chemosonodynamic therapy. *Biomaterials* **234**, 119761 (2020).
65. Cheng, J. et al. Boosting ferroptosis therapy with iridium single-atom nanocatalyst in ultralow metal content. *Adv. Mater.* **35**, 2210037 (2023).
66. Dong, Y. et al. 2D piezoelectric Bi₂MoO₆ nanoribbons for GSH-enhanced sonodynamic therapy. *Adv. Mater.* **33**, 2106838 (2021).
67. Dong, C. et al. A calcium fluoride nanozyme for ultrasound-amplified and Ca²⁺-overload-enhanced catalytic tumor nanotherapy. *Adv. Mater.* **34**, 2205680 (2022).

68. Yin, S. Y. et al. Persistent regulation of tumor microenvironment via circulating catalysis of MnFe_2O_4 @metal-organic frameworks for enhanced photodynamic therapy. *Adv. Func. t Mater.* **29**, 1901417 (2019).
69. Song, G. et al. A large-pore mesoporous Au@Pt@Rh trimetallic nanostructure with hyperthermia-enhanced enzyme-mimic activities for immunomodulation-improved tumor catalytic therapy. *Chem. Eng. J.* **477**, 147161 (2023).
70. Wang, R. et al. Augmenting immunotherapy via bioinspired MOF-based ROS homeostasis disruptor with nanozyme-cascade reaction. *Adv. Mater.* **35**, 2306748 (2023).
71. Cheng, K. et al. Biomimetic material degradation for synergistic enhanced therapy by regulating endogenous energy metabolism imaging under hypothermia. *Nat. Commun.* **13**, 4567 (2022).
72. Shao, C. et al. Epileptic brain fluorescent imaging reveals apigenin can relieve the myeloperoxidase-mediated oxidative stress and inhibit ferroptosis. *Proc. Natl Acad. Sci. USA* **117**, 10155–10164 (2020).
73. Li, K. et al. Multienzyme-like reactivity cooperatively impairs glutathione peroxidase 4 and ferroptosis suppressor protein 1 pathways in triple-negative breast cancer for sensitized ferroptosis therapy. *ACS Nano* **16**, 2381–2398 (2022).
74. Kudarha, R., Dhas, N. & Mutalik, S. Distinct features of iron based metal organic frameworks (MOFs) for ferroptosis mediated cancer therapy: a comprehensive review. *Coord. Chem. Rev.* **494**, 215330 (2023).
75. Kroemer, G., Galluzzi, L., Kepp, O. & Zitvogel, L. Immunogenic cell death in cancer therapy. *Annu. Rev. Immunol.* **31**, 51–72 (2013).
76. Huang, Z. et al. Nanoscale coordination polymers induce immunogenic cell death by amplifying radiation therapy mediated oxidative stress. *Nat. Commun.* **12**, 145 (2021).
77. Obeid, M. et al. Calreticulin exposure dictates the immunogenicity of cancer cell death. *Nat. Med.* **13**, 54–61 (2007).
78. Wang, L. et al. An ER-targeting iridium(III) complex that induces immunogenic cell death in non-small-cell lung cancer. *Angew. Chem. Int. Ed.* **60**, 4657–4665 (2021).
79. Tang, D., Chen, X., Kang, R. & Kroemer, G. Ferroptosis: molecular mechanisms and health implications. *Cell Res* **31**, 107–125 (2021).
80. Kerins, M. J. & Ooi, A. The roles of NRF2 in modulating cellular iron homeostasis. *Antioxid. Redox Signal.* **29**, 1756–1773 (2018).
81. Anandhan, A., Dodson, M., Schmidlin, C. J., Liu, P. & Zhang, D. D. Breakdown of an ironclad defense system: the critical role of NRF2 in mediating ferroptosis. *Cell Chem. Biol.* **27**, 436–447 (2020).
82. Zhong, C.-C. et al. Copper (Cu) induced changes of lipid metabolism through oxidative stress-mediated autophagy and Nrf2/PPAR γ pathways. *J. Nutr. Biochem.* **100**, 108883 (2022).
83. Chen, X., Li, J., Kang, R., Klionsky, D. J. & Tang, D. Ferroptosis: machinery and regulation. *Autophagy* **17**, 2054–2081 (2021).
84. Yang, Y. et al. A two-pronged approach to inhibit ferroptosis of MSCs caused by the iron overload in postmenopausal osteoporosis and promote osseointegration of titanium implant. *Bioact. Mater.* **41**, 336–354 (2024).
85. Fang, X. et al. Ferroptosis as a target for protection against cardiomyopathy. *Proc. Natl Acad. Sci. USA* **116**, 2672–2680 (2019).
86. Kwon, M.-Y., Park, E., Lee, S.-J. & Chung, S. W. Heme oxygenase-1 accelerates erastin-induced ferroptotic cell death. *Oncotarget* **6**, 24393–24403 (2015).
87. Zheng, R. R. et al. Paraptosis inducer to effectively trigger immunogenic cell death for metastatic tumor immunotherapy with IDO Inhibition. *ACS Nano* **17**, 9972–9986 (2023).
88. Song, Y. et al. A bimetallic metal-organic-framework-based biomimetic nanoplateform enhances anti-leukemia immunity via synchronizing DNA demethylation and RNA hypermethylation. *Adv. Mater.* **35**, e2210895 (2023).
89. Zhao, L. et al. Ferroptosis in cancer and cancer immunotherapy. *Cancer Commun.* **42**, 88–116 (2022).
90. Li, T. et al. A pH-activatable copper-biomimetic proenzyme for synergistic chemodynamic/chemo-immunotherapy against aggressive cancers. *Adv. Mater.* **35**, e2210201 (2023).
91. Ye, H. et al. In situ sprayed nanovaccine suppressing exosomal PD-L1 by golgi apparatus disorganization for postsurgical melanoma immunotherapy. *ACS Nano* **17**, 10637–10650 (2023).
92. Kresse, G. & Furthmüller, J. Efficient iterative schemes for ab initio total-energy calculations using a plane-wave basis set. *Phys. Rev. B* **54**, 11169–11186 (1996).
93. Blöchl, P. E. Projector augmented-wave method. *Phys. Rev. B* **50**, 17953–17979 (1994).
94. Perdew, J. P., Burke, K. & Ernzerhof, M. Generalized gradient approximation made simple. *Phys. Rev. Lett.* **77**, 3865–3868 (1996).
95. Hammer, B., Hansen, L. B. & Nørskov, J. K. Improved adsorption energetics within density-functional theory using revised Perdew-Burke-Ernzerhof functionals. *Phys. Rev. B* **59**, 7413–7421 (1999).
96. Grimme, S. Semiempirical GGA-type density functional constructed with a long-range dispersion correction. *J. Comput. Chem.* **27**, 1787–1799 (2006).
97. Damas, G. B., Costa, L. T., Ahuja, R. & Araujo, C. M. Understanding carbon dioxide capture on metal-organic frameworks from first-principles theory: The case of MIL-53(X), with X = Fe^{3+} , Al^{3+} , and Cu^{2+} . *J. Chem. Phys.* **155**, 024701 (2021).
98. Nørskov, J. K. et al. Origin of the overpotential for oxygen reduction at a fuel-cell cathode. *J. Phys. Chem. B* **108**, 17886–17892 (2004).

Acknowledgements

This work was supported by the funding from National Natural Science Foundation of China (No. 22207011 to Y.B., 22375026 to J.W.) and Changzhou Leading Innovative Talents Introduction and Cultivation Project (CQ20220085 to Y.B.).

Author contributions

Y.B., H.P. and J.W. conceived the research. Z.Y. and Y.B. wrote the manuscript. Z.Y., L.K., Y.W., S.Z., H.S., Yi.L., L.Q., R.Z. and Z.C. designed and conducted the experiments. D.Z., and Z.C. provided technical supports and helped with the investigations. Y.B., L.Q., P.J., Yafei.L., H.P. and J.W. supervised this study and revised the manuscript. All authors discussed the experimental results and approved the final manuscript. Correspondence and requests for materials should be addressed to Yang Bai, Yafei Li, Huan Pang or Jianhao Wang.

Competing interests

The authors declare no competing interests.

Additional information

Supplementary information The online version contains supplementary material available at <https://doi.org/10.1038/s41467-025-57542-x>.

Correspondence and requests for materials should be addressed to Yang Bai, Yafei Li, Huan Pang or Jianhao Wang.

Peer review information *Nature Communications* thanks Priscila Fala-gan Lotsch, Gan Tian and the other, anonymous, reviewer(s) for their contribution to the peer review of this work. A peer review file is available.

Reprints and permissions information is available at <http://www.nature.com/reprints>

Publisher's note Springer Nature remains neutral with regard to jurisdictional claims in published maps and institutional affiliations.

Open Access This article is licensed under a Creative Commons Attribution-NonCommercial-NoDerivatives 4.0 International License, which permits any non-commercial use, sharing, distribution and reproduction in any medium or format, as long as you give appropriate credit to the original author(s) and the source, provide a link to the Creative Commons licence, and indicate if you modified the licensed material. You do not have permission under this licence to share adapted material derived from this article or parts of it. The images or other third party material in this article are included in the article's Creative Commons licence, unless indicated otherwise in a credit line to the material. If material is not included in the article's Creative Commons licence and your intended use is not permitted by statutory regulation or exceeds the permitted use, you will need to obtain permission directly from the copyright holder. To view a copy of this licence, visit <http://creativecommons.org/licenses/by-nc-nd/4.0/>.

© The Author(s) 2025